



# Numerical Investigation on Anisotropy and Shape Effect of Mechanical Properties of Columnar Jointed Basalts Containing Transverse Joints

Yongyi Wang<sup>1</sup> · Bin Gong<sup>2</sup> · Chun'an Tang<sup>1</sup>

Received: 8 November 2021 / Accepted: 27 May 2022 / Published online: 15 August 2022  
© The Author(s) 2022

## Abstract

We studied the non-linear mechanical response and failure mechanism of columnar jointed basalts (CJBs) with transverse joints by modeling meso-mechanics, statistical damage theory and continuum mechanics. The anisotropy and shape effect of CJBs with transverse joints were captured under different lateral pressures. The digital images were transformed into heterogeneous element meshes, and the gradual fracturing process and various failure modes of CJBs were reproduced. The compressive strength (CS) and equivalent deformation modulus (EDM) of CJBs parallel and perpendicular to the column axis were studied. The results show that the U-shaped CS curve of CJB appears as the column dip angle increases, and the CS is obviously improved as the lateral pressure increases when the column dip angle is  $0^{\circ}$ – $90^{\circ}$ . When the shape of CJB changes from  $6\text{ m} \times 3\text{ m}$ ,  $3\text{ m} \times 3\text{ m}$  to  $1.5\text{ m} \times 3\text{ m}$ , the CS continues to increase. Meanwhile, the transverse joints are proven to be critical for determining the mechanical properties of CJBs at the certain dip angles of columns. However, the high lateral pressure can reduce the CS difference between the CJBs with and without the transverse joints. Besides, as the elastic modulus of joints rises, the CS will grow up, and the EDM will increase first and then almost remain at the same level. The coefficient of rock residual strength has a great influence on the CS at the certain dip angles of columns. Additionally, the model boundary significantly affects the anisotropy and shape effect of mechanical properties of CJBs under compression. These conclusions will improve our knowledge of the failure mechanisms and failure patterns of CJBs containing transverse joints.

## Highlights

- Transverse joints greatly affect the anisotropy and shape effect of CJBs
- High lateral pressure can reduce the CS difference between CJBs with and without transverse joints
- The U-shaped CS curve of CJB generally appears as the column dip angle increases

**Keywords** Columnar jointed basalts · Transverse joints · Anisotropy · Shape effect · Numerical simulation

## 1 Introduction

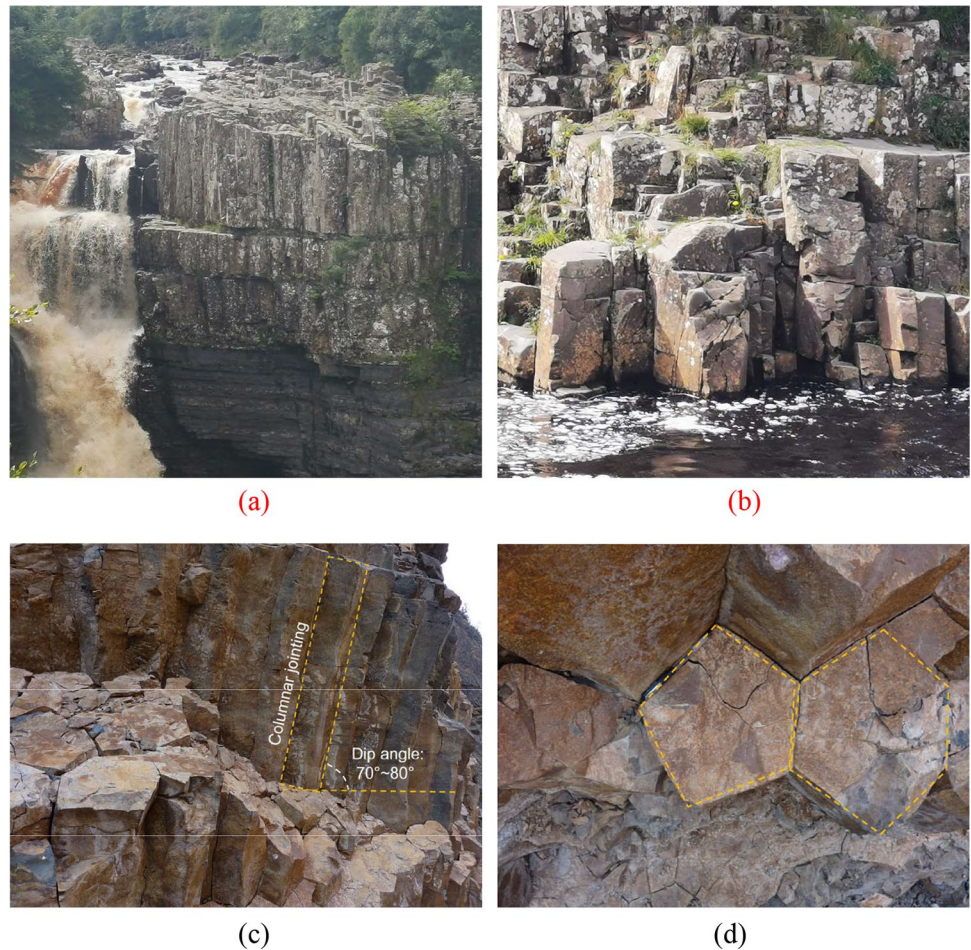
Columnar joints are a kind of fracturing networks caused by cold shrinkage of erupted basalts. They often cut rock mass into regular or irregular prisms, forming columnar jointed basalts (CJBs) or columnar jointed rock masses (CJRM). CJBs have been found at many places on the earth, such as the United States, Australia, China, Brazil, India, Scotland, and Siberia (Gilman 2009; Guy 2010; Zavada et al. 2015; Huang et al. 2020; Weinberger and Burg 2019). In recent decades, many large-scale infrastructures related to CJBs have been constructed or planned in the southwestern part of

✉ Bin Gong  
bin.gong@brunel.ac.uk

<sup>1</sup> State Key Laboratory of Coastal & Offshore Engineering, Dalian University of Technology, Dalian 116024, China

<sup>2</sup> Department of Civil and Environmental Engineering, Brunel University London, London UB8 3PH, UK

**Fig. 1** The observed CJBs/CJRM in the field: **a** at the Low Force Waterfall, Durham, UK; **b** at the High Force Waterfall, Durham, UK; **c** and **d** at the Baihetan Hydroelectric Station in China (Ji et al. 2017)



China, such as the Longkaikou Hydroelectric Station located in the middle reaches of Jinsha River with extra-long traffic tunnels. The observed CJBs/CJRM in the field can be seen in Fig. 1.

In terms of mechanical properties of CJRM (or CJBs), some researchers have carried out relevant studies. In the aspect of numerical simulation, the conventional numerical methods are generally difficult to simulate the progressive fracture process of CJRM (Simo and Ju 1987; Lemaitre 1992; Skrzypek and Ganczarski 1999; Lemaitre and Desmorat 2005). For instance, Yan et al. (2012) investigated the macroscopic equivalent elastic moduli of CJRM by the three-dimensional (3D) discrete element method (DEM). But the gradual fracture behaviors were not displayed and analyzed. Zheng et al. (2010) discussed the anisotropy and size effect of CJRM using the deformable DEM models with different sizes. However, the fracture-induced acoustic emission (AE) characteristics of CJRM were not captured and discussed. Cui et al. (2016) analyzed the influence of structural characteristics on the equivalent deformation moduli (EDMs) of CJRM by the finite element method (FEM). Nevertheless, the variation of stress field during fracture process was not depicted and investigated. Based

on the 3D finite difference method (FDM), Yan et al. (2018) simulated the mechanical behavior of CJRM with various column angles and investigated the deformation and strength features of the CJRM under true triaxial compression. However, the fracture-induced AE precursors of CJRM were not revealed. In general, the above numerical simulations have made beneficial progress about the anisotropy and size effect of CJRM. But, the effect of lateral pressures on the fracture mechanism and AE characteristics of CJRM (or CJBs) with different shapes has not been fully understood.

In the aspect of experimental test, it is generally difficult to make the CJRM (or CJBs) samples with transverse joints and consider the mechanical properties of real joints. Ji et al. (2017) performed the uniaxial compression tests on CJRM samples composed of cement, fine sand, water as well as water-reducer. They further analyzed the fracture modes of CJRM by varying column angle. However, the influence of mechanical property variation of joints was not taken into account. Xiao et al. (2014 and 2015a) gained the various deformation and strength parameters of CJBs by varying column angle and discussed the anisotropic features by the compression tests. Nevertheless, in their study, the cement paste was used to bond the columns, which were

different from the real joints of CJRMs. Ke et al. (2019) investigated the effect of column angles and transverse joints on the mechanical parameters and fracturing mechanisms of CJRMs. However, the AE characteristics underlying the fracture process of CJRMs were not studied. Lin et al. (2018) analyzed the shape effect of CJRM specimens with transverse joints by laboratory physical experiments and obtained the curves of uniaxial compressive strengths (UCSs) with various shapes and column dip angles, but the energy evolution and the influence of lateral pressure were not considered. Overall, the physical tests have obtained valuable research results on the understanding of mechanical properties of CJRMs. However, when more environmental factors need to be considered, the laboratory physical test will be time-consuming and uneconomic.

In the aspect of field test, a series of valuable achievements concerning the mechanical properties of CJBs (or CJRMs) have been obtained although the occurrence environment of engineering rock mass in the field is complicated. Jiang et al. (2013 and 2018) carried out field investigation on the anisotropic characteristics of CJBs. However, due to the limitation of field condition, the systematic research on shape effect of CJBs was difficult to carry out. Xiao et al. (2017) captured the microseism signals resulting from the excavation of the CJBs at a hydroelectric station, but the signals were probably affected by various factors. Fan et al. (2018) investigated the unloading relaxation and rebound deformation of CJBs by in situ testing. Nevertheless, the influence of joint mechanical properties and rock constitutive relation were difficult to consider in field test. Xia et al. (2020a, b) investigated the geometric configuration of CJB and their influence on the P-wave anisotropy at the Baihetan Hydroelectric Station. However, due to the environmental limitation, it was not convenient to study the shape effect of CJBs. Although many researchers have studied the mechanical properties of CJBs by means of field test, laboratory physical test and numerical simulation, the mechanical properties and AE characteristics of CJBs with different shapes have not been fully understood. Meanwhile, the research of the fracture mechanisms of CJBs with different shapes and transverse joints is insufficient.

The mechanical behavior and instability precursor of underground cavern CJB wall with different height–width ratios are closely related with the shape effect of CJBs. Simultaneously, the determination of the mechanical parameter values used in the stability analysis of CJB engineering is also affected by the shape effect of CJB specimens. To understand the anisotropy, shape effect and fracture mechanism of CJBs with transverse joints, the meso-mechanics, and statistical damage theory were modeled in this study. A group of inhomogeneous CJB models with various specimen shapes and transverse joints was established. Under lateral pressure, the effects of transverse joints, joint mechanical

parameters, rock constitutive relations and boundary conditions were numerically simulated and concluded.

## 2 Methods

### 2.1 The RPFA Code Enhanced by DIC

The advantage of the rock failure process analysis (RPFA) code is to simulate the gradual fracture process without the hypotheses about how and where new microcracks will initiate and develop (Tang and Kou 1998; Liang 2005; Feng et al. 2022). Additionally, the effectiveness of RPFA has been verified by many benchmarks (Xu et al. 2021; Wang et al. 2022). Meanwhile, RPFA has been applied in the stability assessment (Chen et al. 2022; Gong et al. 2022a), failure mechanism (Zhou et al. 2018; Gong et al. 2022b) and instability precursor (Liu et al. 2017; Zhang et al. 2021) of rock mass.

The model-building ability of RPFA was improved by the digital image correlation (DIC) technology. First, the model data carried by an image consisting of square pixels needs to be transformed into the related parameter matrixes. Assuming that the image has a certain thickness, the square pixels can be treated as numerous finite elements, and their node coordinates will be determined according to the spatial positions of the linked pixels. Second, the element attributes can be assigned by distinguishing the grayscale of every pixel and classifying it into the corresponding joint or rock materials. The construction process of a heterogenous model has been presented in Fig. 2. According to the statistical damage mechanics, the mechanical parameters of finite elements are presumed to obey a given Weibull distribution to represent the inhomogeneity of rock masses. Thirdly, the Mohr–Coulomb strength criterion with tension cut-off is applied as the strength criterion. Clearly, if the minor principal stress of an element reaches the uniaxial tensile strength, the tensile damage would occur, while the stresses of an element reach the Mohr–Coulomb strength criterion, the compression–shear damage would happen (illustrated by Fig. 3). Fourthly, the bearing ability of a meso-element is going to decrease as the damage evolves and remain a specific residual strength after reaching the strength criteria. Based on the approach developed by Mazars and Pijaudier-Cabot (1989), the stress–strain relationship displayed in Fig. 3 can be extended to the 3D stress space.

### 2.2 The Damage Evolution of Meso-elements

For the DIC-enhanced RPFA method, the meso-elements will be linear elastic at the beginning, which are described using Young's modulus and Poisson's ratio. After the

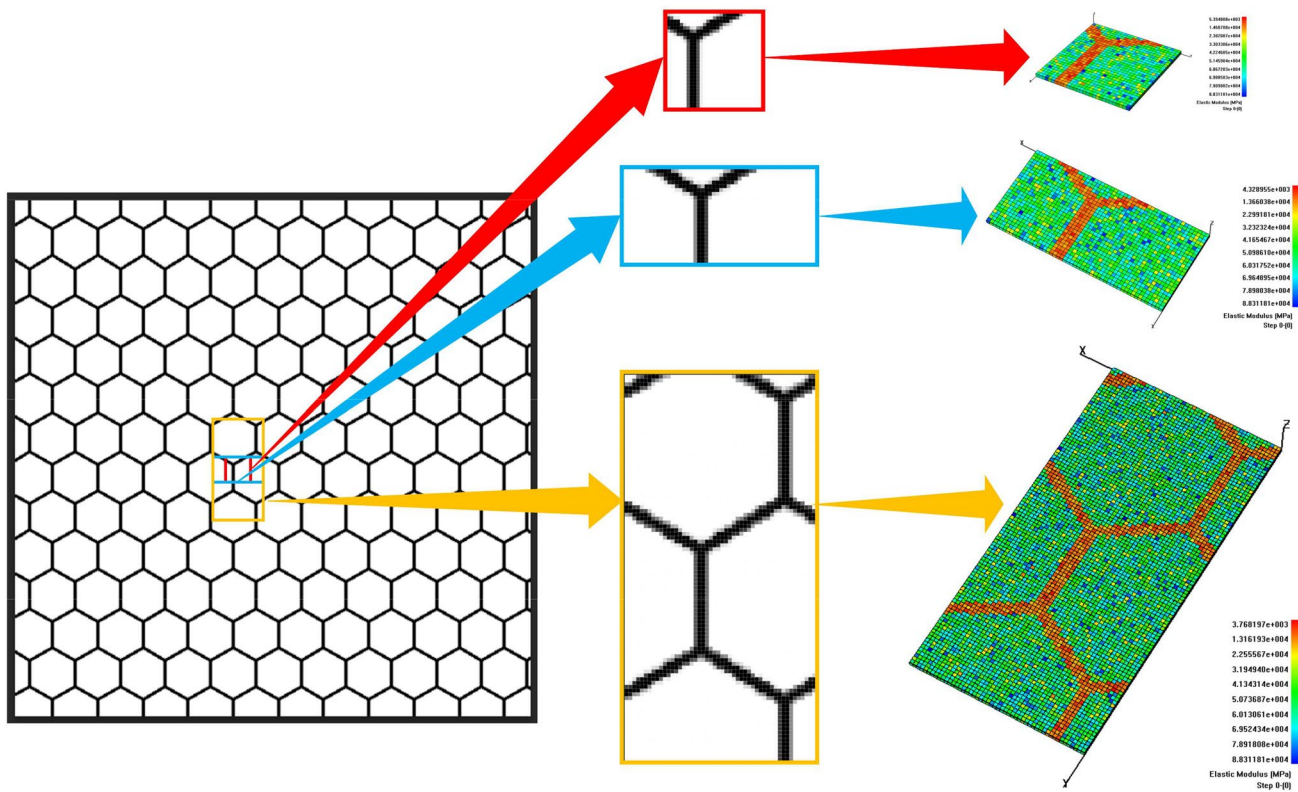
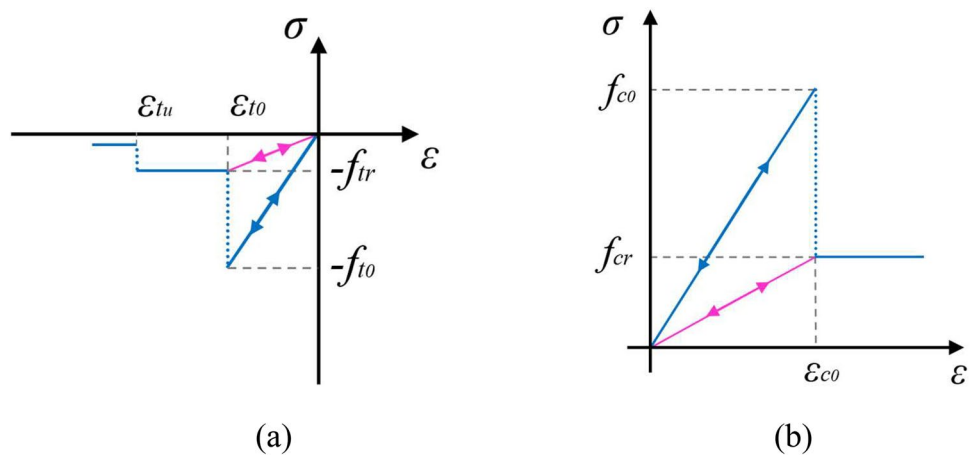


Fig. 2 Schematic diagram of transforming digital image into heterogeneous numerical model

Fig. 3 Elastic-brittle damage constitutive relation of an element under uniaxial stress: **a** tensile state and **b** compressive state



specific failure criterion is satisfied, the constitutive curve will be modified by softening. For the Mohr–Coulomb strength criterion with tension cut-off, when a meso-element is subjected to uniaxial tension, the elastic-brittle-plastic stress–strain curve is applied. The tensile failure threshold could be expressed as follows:

$$\sigma_3 \leq -f_t, \tag{1}$$

where  $f_t$  represents the uniaxial tensile strength, and the tensile stress and strain are negative.

Meanwhile, the Mohr–Coulomb strength criterion is adopted for judging if the element damages in the compression-shear mode, as follows:

$$\sigma_1 - \frac{1 + \sin\varphi}{1 - \sin\varphi} \sigma_3 - f_c \geq 0, \tag{2}$$

where  $\sigma_1$  and  $\sigma_3$  represent the maximum and minimum principal stresses;  $\varphi$  and  $f_c$  represent the internal friction angle and UCS.

Besides, if the stress state exceeds the specific state causing element failure, the elastic modulus of the meso-element would degenerate with the damage evolving, which is able to be described using Eq. (3).

$$E = (1 - D)E_0, \tag{3}$$

where  $D$  is termed the damage coefficient;  $E_0$  and  $E$  are the initial and degenerated elastic moduli of the meso-element, respectively.

According to the damage mechanics, when the tension damage happens, the damage coefficient  $D$  could be determined using Eq. (4) (Tang et al. 2015):

$$D = \begin{cases} 0 & \varepsilon > \varepsilon_{t0} \\ 1 - \frac{\lambda\varepsilon_{t0}}{\varepsilon} & \varepsilon_{tu} < \varepsilon \leq \varepsilon_{t0} \\ 1 & \varepsilon \leq \varepsilon_{tu} \end{cases}, \tag{4}$$

where  $\lambda (=f_{tr}/f_t)$  represents the residual strength coefficient;  $f_t$  and  $f_{tr}$  represent the uniaxial and residual tensile strengths;  $\varepsilon_{t0} (=f_t/E_0)$  represents the limit tensile elastic strain, and  $\varepsilon_{tu} (= \eta\varepsilon_{t0})$  is the ultimate tensile strain occurring when the element damages completely;  $\eta$  is the ultimate tensile strain coefficient.

Moreover, when the element damages in the compression-shear mode,  $D$  could be determined using Eq. (5) (Tang et al. 2015):

$$D = \begin{cases} 0 & \varepsilon < \varepsilon_{c0} \\ 1 - \frac{\lambda\varepsilon_{c0}}{\varepsilon} & \varepsilon \geq \varepsilon_{c0} \end{cases}, \tag{5}$$

where  $\lambda (=f_{cr}/f_c)$  is the residual strength coefficient;  $f_c$  and  $f_{cr}$  represent the uniaxial and residual compressive strengths;  $\varepsilon_{c0} (=f_c/E)$  represents the limit compressive elastic strain. Furthermore, the analysis process is illustrated by Fig. 4.

### 2.3 Benchmark

The laboratory tests conducted by Xiao et al. (2014) and Ji et al. (2017) were used to prove the effectiveness of the RFPA approach. According to Xiao et al. (2014), the cylindrical CJB samples whose diameter and height were 50 mm

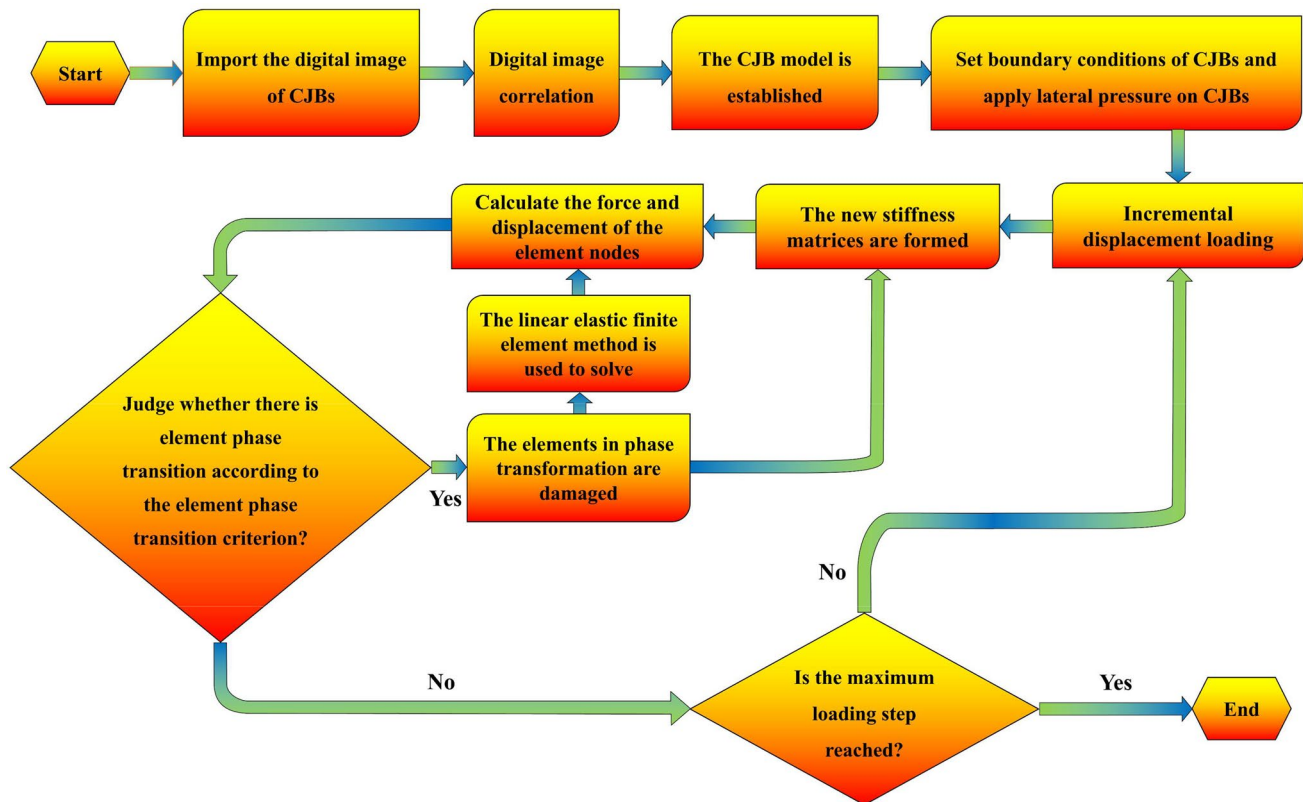
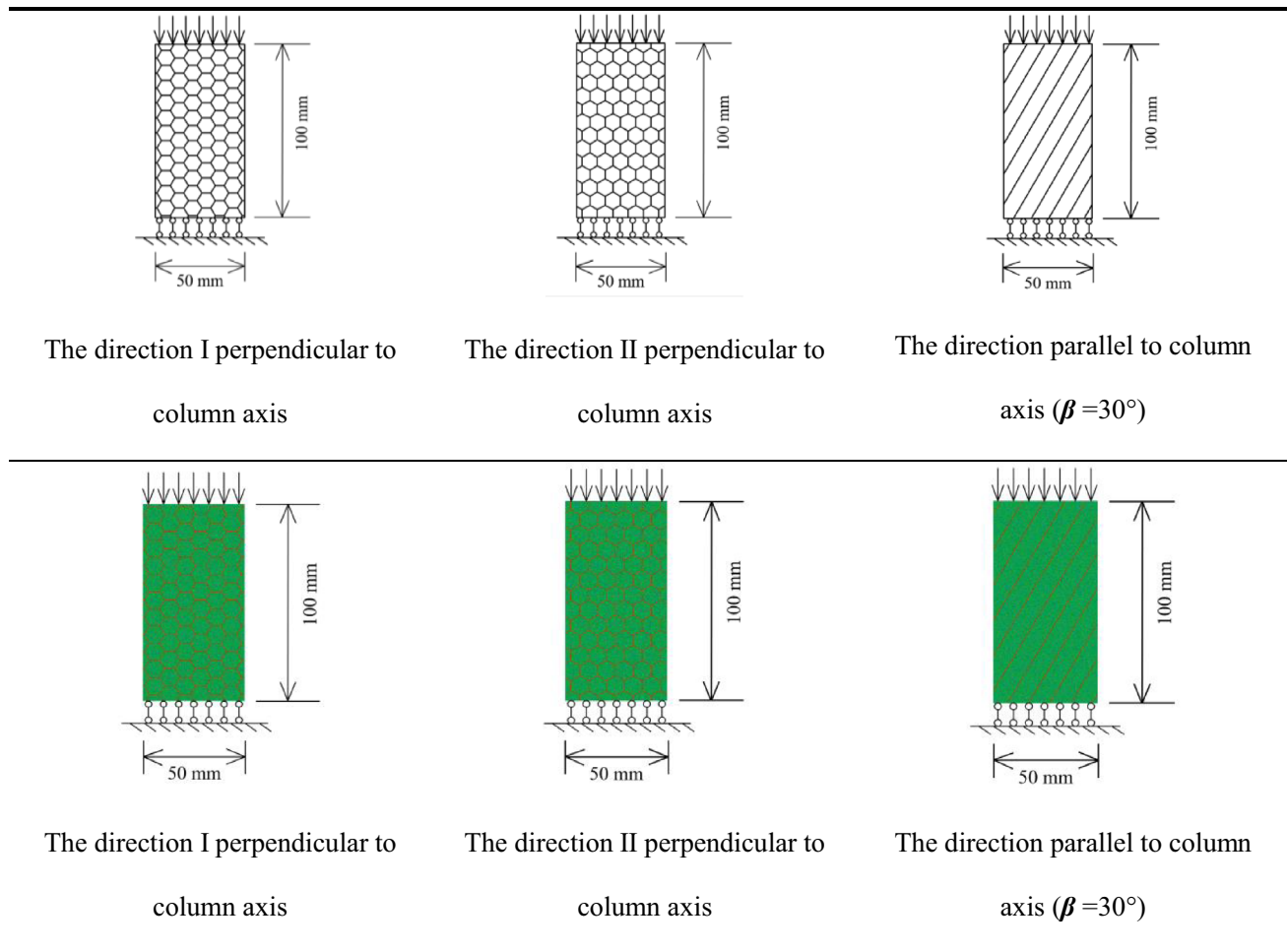


Fig. 4 Calculation flow of the DIC-enhanced RFPA method

**Table 1** Model geometry, joint setting and loading condition under uniaxial compression for numerical verification**Table 2** Mechanical parameters of finite element model for numerical verification

Material type	Heterogeneity index	Elastic modulus (GPa)	Uniaxial compressive strength (MPa)	Poisson's ratio	Friction angle ( $^\circ$ )	Residual strength coefficient
Basalt	5	60	120	0.2	56.15	0.1
Joint	5	15	30	0.25	36	1

and 100 mm were produced using gypsum, cement and water with the mass ratio of 3:1:3.2. A series of uniaxial compression tests were performed by the MTS815 servo-controlled testing machine. Meanwhile, the samples owning the same size were made by Ji et al. (2017) using cement, fine sand, water and water-reducer with the mass ratio of 1:0.5:0.35:0.002. The corresponding compression tests were conducted as well.

In this study, the related numerical samples with the size of 50 mm (width)  $\times$  100 mm (height) were built up by converting the digital images. The inner hexagonal prisms had the diameter of 10 mm. The different sections with different

normal directions parallel and perpendicular to the column axis were considered, as displayed in Table 1. The used physico-mechanical parameters were from the relevant literature (Fan et al. 2018; Ke et al. 2019; Xiao et al. 2017; Yan et al. 2012; Zheng et al. 2010), as listed in Table 2. The loading was performed using the rate of 0.005 mm/step until the macroscopic instability of a sample.

The normalized UCS coefficients of the experiments and the simulations, which are defined as the macroscopic strengths of the samples divided by the mesoscopic strengths of the materials, are displayed in Fig. 5. Additionally, Fig. 5

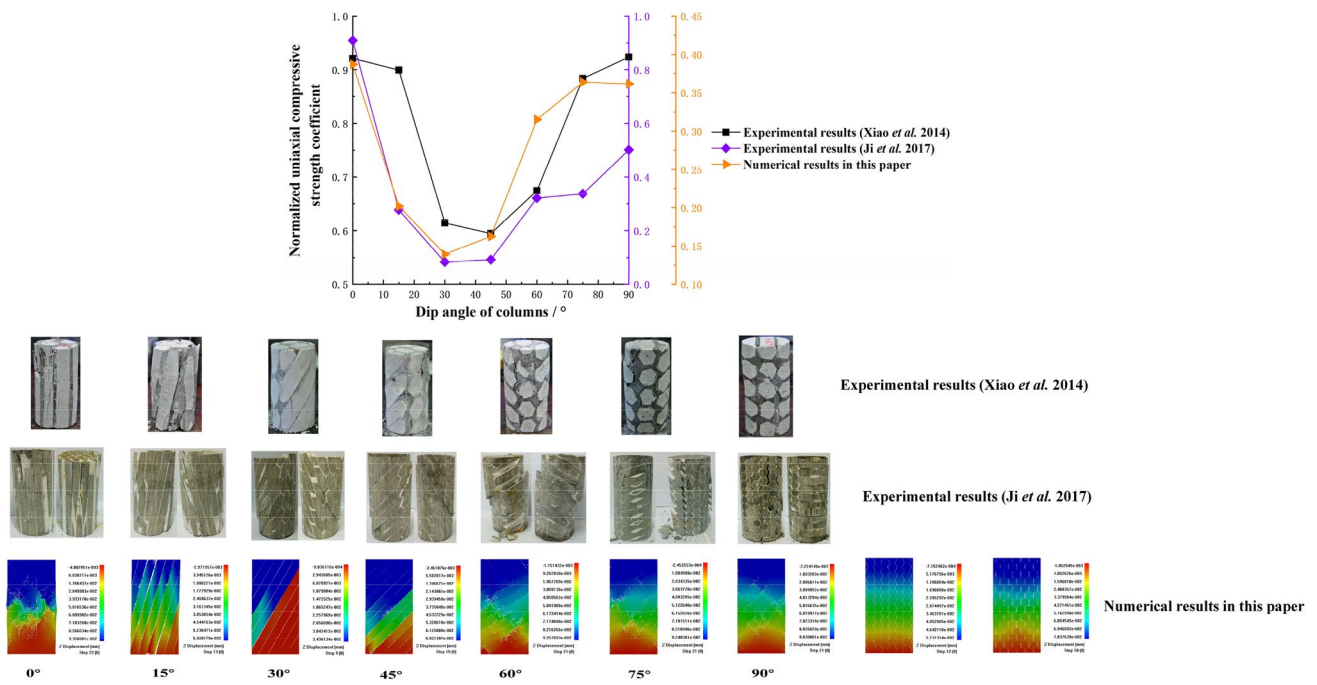


Fig. 5 Comparison of normalized uniaxial compression strength coefficients and failure modes obtained by experiment and simulation

shows that the simulated failure modes agree with the experimental results very well.

### 2.4 Model Configuration

By referring to the CJBs encountered at the Baihetan Hydroelectric station in Southwest China, the model geometry and boundary conditions were determined, as listed in Table 3. The elastic moduli of joints are displayed in Fig. 6a. Meanwhile, the residual strength coefficients of intact rock, reflecting the continuous change of rock material from brittleness to plasticity can be seen in Fig. 6b. Besides, the spacing and distance ratio of the secondary joint set were 1.5 m and 50%, respectively. In the aspect of model boundary, the case between plane stress and plane strain and the case of plane strain were considered.

In the simulations, the element size of each model was the same. By taking the 6 m × 3 m model as an example, the total element number was 1,216,800. Figure 7a shows the diagrams of the 1.5 m × 3 m and 6 m × 3 m models along the direction perpendicular to the column axis; Fig. 7b depicts some details of the 6 m × 3 m model with and without transverse joints, along the direction parallel to the column axis. Meanwhile,

the two kinds of boundary conditions are shown in Fig. 7c and d. For the situation between plane stress and plane strain, the deformation constrains were put along the positive normal direction of the section, which represented rock masses with a free surface, like the walls of a tunnel moving towards the free face, as presented in Fig. 7c. For the situation of plane strain, the deformation constrains were put along both the positive and negative normal directions of the section, which represented rock masses without deformation along a specific direction, like surrounding rock masses along the axis of a tunnel, as depicted in Fig. 7d. The displacement-controlled loading was performed on the model top vertically.

Generally, considering that the strengths of joints are weaker than intact rocks, the joint parameters can affect the deformation modulus and macroscopic strength of CJBs (Gui and Zhao 2015 and Sun et al. 2012). According to the previous simulations and relevant literature (Fan et al. 2018; Ke et al. 2019; Xiao et al. 2017; Yan et al. 2012; Zheng et al. 2010), the physico-mechanical properties of joints were chosen, as shown in Table 4.

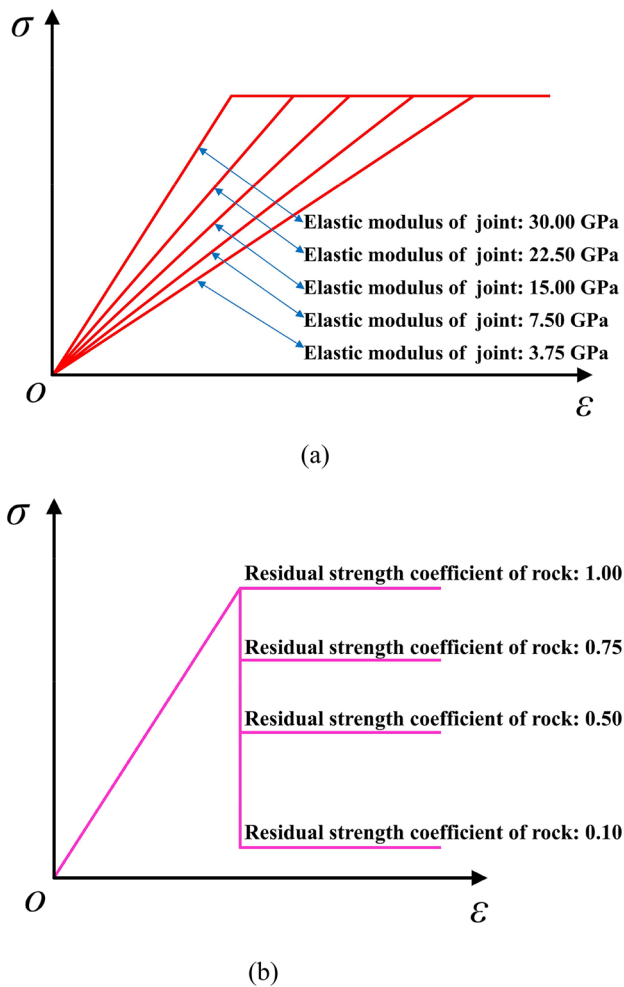


**Fig. 6** **a** The constitutive relation of joint with different elastic moduli and **b** the constitutive relation of rock with different residual strength coefficients

### 3 Results

#### 3.1 Anisotropy and Shape Effect of CJBs with Transverse Joints

We can see from Fig. 8a that for the  $1.5 \text{ m} \times 3 \text{ m}$  sample with transverse joints, as the lateral pressure increases, the compressive strengths (CSs) of the samples at the dip angles of  $0^\circ \sim 90^\circ$  are obviously improved. In addition, compared with the  $1.5 \text{ m} \times 3 \text{ m}$  and  $3 \text{ m} \times 3 \text{ m}$  samples, the CSs of  $3 \text{ m} \times 3 \text{ m}$  specimens are relatively low if the lateral pressure reaches 6 MPa and the dip angles of columns are  $0^\circ \sim 90^\circ$ . Figure 8b indicates that for the  $1.5 \text{ m} \times 3 \text{ m}$  sample with transverse joints, compared with the other confining pressures, the equivalent deformation moduli (EDMs) of the samples are relatively low if the lateral pressure is 0 MPa and the dip angles are  $0^\circ \sim 30^\circ$  and  $75^\circ \sim 90^\circ$ . The EDMs of the samples fluctuate greatly at the

dip angles of  $0^\circ \sim 90^\circ$  after the lateral pressure reaches 2 MPa. With the lateral pressure rising to 4–8 MPa, the EDMs of the samples firstly decrease and then increase slightly as the dip angle grows up.

As presented in Fig. 8c, for the  $6 \text{ m} \times 3 \text{ m}$  specimen with transverse joints, as the lateral pressure increases, the CSs of the samples are obviously improved at the dip angles of  $0^\circ \sim 90^\circ$ . Meanwhile, the CS of the model with the column dip angle of  $60^\circ$  decreases after the lateral pressure exceeds 6 MPa. However, the model CSs with the other column dip angles still increase obviously. In addition, it can be found that compared with the  $3 \text{ m} \times 3 \text{ m}$  and  $6 \text{ m} \times 3 \text{ m}$  specimens, the CSs of the  $3 \text{ m} \times 3 \text{ m}$  and  $6 \text{ m} \times 3 \text{ m}$  specimens show a little difference at the dip angle of  $45^\circ$  when the lateral pressure = 6 MPa, while the CSs of the  $3 \text{ m} \times 3 \text{ m}$  specimens are larger at the other dip angles. For the  $6 \text{ m} \times 3 \text{ m}$  specimen with transverse joints, compared with the other lateral pressures, the EDMs of the specimens at the dip angles of  $0^\circ$  and  $75^\circ$  are relatively low if the lateral pressure = 0 MPa, as depicted in Fig. 8d. When the lateral pressure rises to 2–8 MPa, as the column dip angle increases, the EDMs of the samples basically decrease (or decrease in a fluctuating way) and then slightly increase.

Figure 9 shows the  $z$ -direction displacement diagrams of the  $1.5 \text{ m} \times 3 \text{ m}$  and  $6 \text{ m} \times 3 \text{ m}$  CJBs with transverse joints when the lateral pressures = 0 MPa and 4 MPa and  $\beta = 0^\circ, 30^\circ, 60^\circ$  and  $90^\circ$ . Figure 9a and e shows that when the lateral pressure = 0 MPa and  $\beta = 0^\circ$ , for the  $1.5 \text{ m} \times 3 \text{ m}$  sample with transverse joints, most of the columnar joints inside the sample get damaged, and the cracks in the specimen are unevenly distributed. When the lateral pressure is 4 MPa, except that a columnar joint at the left side of the specimen shows local fracture, there is no obvious fracture at the rest area of the model, and the sedimentation in the specimen is relatively evenly distributed. Figure 9b and f shows that when the lateral pressure = 0 MPa and  $\beta = 30^\circ$ , for the  $1.5 \text{ m} \times 3 \text{ m}$  sample, most of the columnar joints are slipped and cracked. Simultaneously, some transverse joints are also damaged. At the edges of some columns, new cracks generate and develop, and the sedimentation in the specimen is evenly distributed. The cracking of columnar joints inside the specimen is not obvious when the lateral pressure equals 4 MPa. Near the lower left and middle upper areas of the sample, several columns are broken, and the sedimentation is unevenly distributed. Figure 9c and g shows that when the lateral pressure = 0 MPa and  $\beta = 60^\circ$ , for the  $1.5 \text{ m} \times 3 \text{ m}$  sample, the transverse joints inside the specimen get cracked, and the sedimentation in the specimen is symmetrically distributed. The fracture trend and sedimentation distribution in the specimen are similar when the lateral pressure are 0 MPa and 4 MPa. Figure 9d and h shows that when the lateral pressure = 0 MPa and  $\beta = 90^\circ$ , for the  $1.5 \text{ m} \times 3 \text{ m}$  sample, there

are several transverse joints damaged inside the specimen. Additionally, the fractures of columns are obvious at the left and right parts of the sample. Meanwhile, the sedimentation distribution is basically uniform. Under the lateral pressure of 4 MPa, there are no obvious cracks at the transverse joints, but the fractures of columns is also obvious at the left and right parts of the sample, and the sedimentation distribution is still basically uniform.

As shown in Fig. 9 i and m, when the lateral pressure = 0 MPa, for the  $6\text{ m} \times 3\text{ m}$  and  $\beta = 0^\circ$  model with transverse joints, most of the columnar joints at the middle of the sample are damaged. Simultaneously, there is an inverted V-shaped fracture zone at the center of the sample, and the sedimentation is distributed along the inverted V-shaped fracture zone. Furthermore, the cracked columnar joints at the center of the sample become less, the inverted V-shaped fracture zone is not less obvious, and the sedimentation distribution is more uniform under the lateral pressure of 4 MPa. Figure 9 j and n shows that when the lateral pressure = 0 MPa, for the  $6\text{ m} \times 3\text{ m}$  and  $\beta = 30^\circ$  sample, in addition to the slip cracking of columnar joints, there are several transverse joints cracked, and the sedimentation in the specimen is distributed along the columnar joints. After the lateral pressure increases to 4 MPa, the transverse joints in the specimen are not cracked obviously, but the sedimentation distribution in the specimen is similar with the lateral pressure of 0 MPa. According to Fig. 9 k and o, for the  $6\text{ m} \times 3\text{ m}$  and  $\beta = 60^\circ$  sample subjected to the lateral pressure of 0 MPa, there are many transverse joints cracked inside the specimen, and the cracks propagate along the original direction, and the sedimentation is distributed along the fracture zone. After the lateral pressure reaches 4 MPa, the cracked transverse joints are less, the fracture zone is also less obvious, and the sedimentation distribution is more uniform. In Fig. 9 l and p, when the lateral pressure = 0 MPa, for the  $6\text{ m} \times 3\text{ m}$  and  $\beta = 90^\circ$  sample, several transverse joints in the middle of the specimen get cracked, and there is an inverted V-shaped fracture zone at the center of the sample. If the lateral pressure rises to 4 MPa, there are no transverse joints cracked in the middle of the sample, but the inverted V-shaped fracture zone still exists in the middle of the sample, and the sedimentation distribution remains relatively uniform.

## 3.2 Progressive Fracture Process and Failure Pattern of CJBs with Transverse Joints

### 3.2.1 Along the Direction I Perpendicular to the Column Axis

- (1) For the  $1.5\text{ m} \times 3\text{ m}$  model subjected to the lateral pressure of 0 MPa.

Figure 10 a and b shows the stress–strain relationship and AE curve of  $1.5\text{ m} \times 3\text{ m}$  model under the lateral pressure of 0 MPa. Figure 10 c and d shows the minor principal stress contours at the Points C and F of the stress–strain relationship, describing the generation and growth of cracks under continuous load. We can see that at the Point B, the vertical joints in the sample are cracked firstly with the load increasing, and there are high stresses concentrated at the centers of the columns. Furthermore, the vertical joints within the sample get damaged more seriously at the stress-peak Point C, and the obvious stress concentrations are intensified at the columns. With the stress falling to the Point D, numerous cracks generate at column centers and propagate at the middle upper, lower left and right parts of the sample. However, the concentrated stresses at the other columns decrease. After the stress continues to drop to the Point E, those cracks in the columns propagate, and the stress concentrations in the sample further weaken. At the Point F, the broken columns get cracked seriously. Additionally, as depicted in Fig. 10 b, the AE rate is distributed in the single peak trend, and the maximum AE value is mainly induced by the macroscopic rupture of columns.

- (2) For the  $1.5\text{ m} \times 3\text{ m}$  model subjected to the lateral pressure of 6 MPa.

Figure 10 e and f displays the stress–strain relationship and AE curve of  $1.5\text{ m} \times 3\text{ m}$  model under the lateral pressure of 6 MPa. Figure 10 g and h shows the minor principal stress contours at the Points C and F of the stress–strain relationship. There are weak stress concentrations at the vertical joints at the load Point A. After the stress increases to the Point B, we can see that there are different degrees of stress concentrations at the columns within the left and right parts of the model, especially in the left part where the stress concentrations are more obvious. At the peak Point C, at the left side of the sample, the previous high stresses are increased and lead to more and more crack initiation and propagation. After the load drops to the Point D, more columns are cracked in the lower left area of the sample. Besides, the high stresses and new cracks appear at the columns in the right area of the model. At the Point E, the previously concentrated stresses decrease in the left area

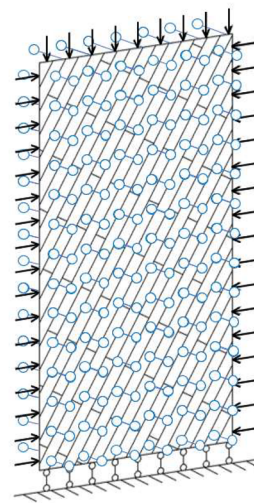
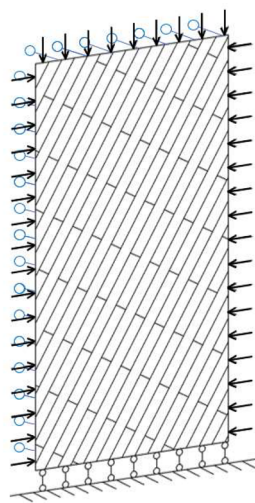
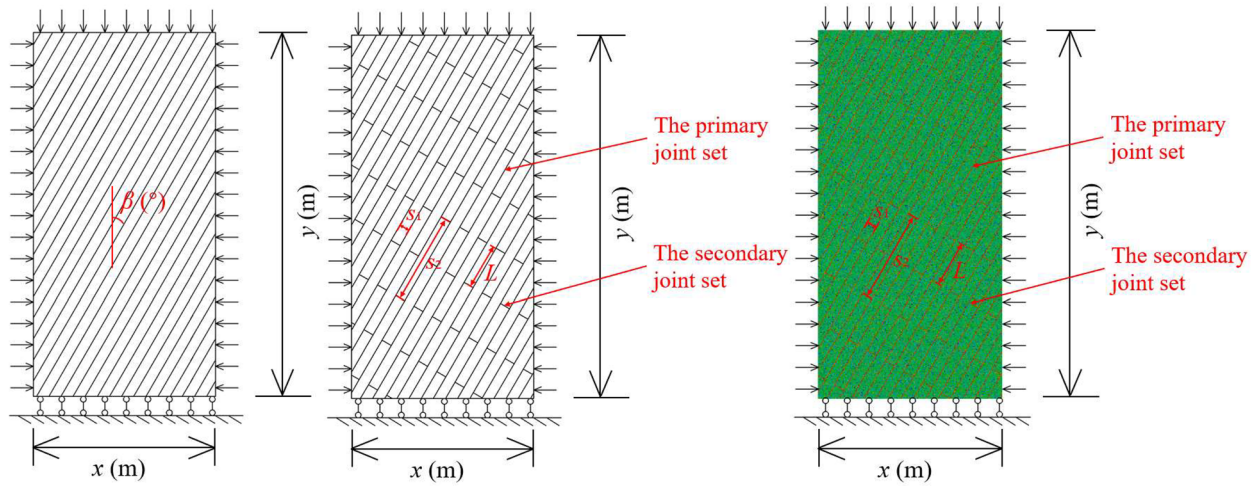
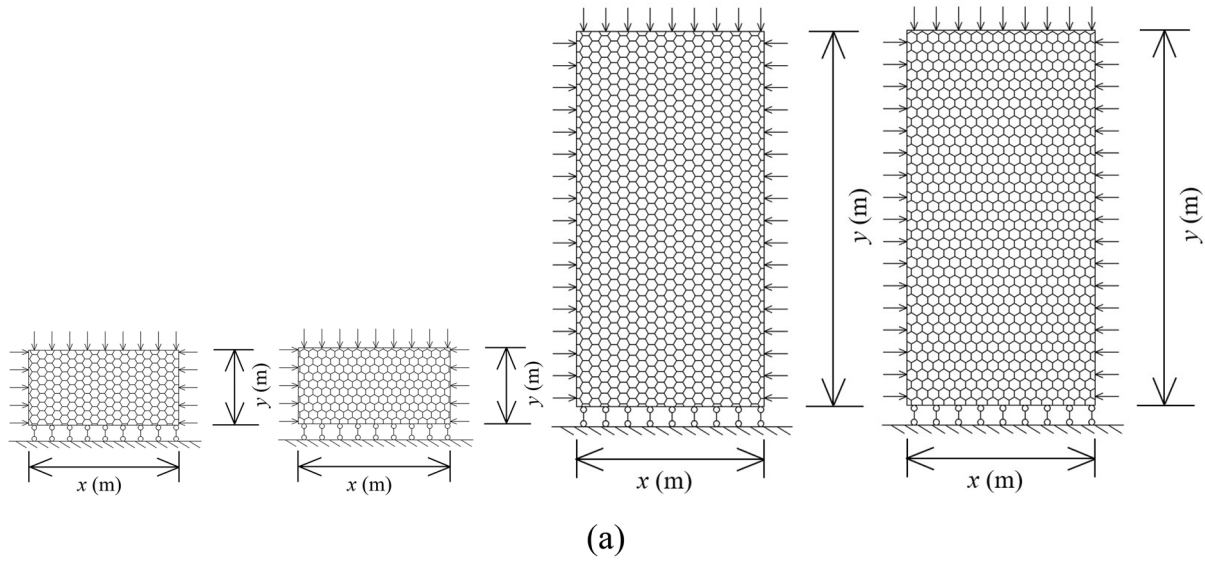


**Fig. 7** **a** Diagram of the  $1.5 \text{ m} \times 3 \text{ m}$  and  $6 \text{ m} \times 3 \text{ m}$  CJBs with transverse joints, along the direction perpendicular to column axis; **b** diagram and boundary condition of the  $6 \text{ m} \times 3 \text{ m}$  CJBs without and with transverse joints, along the direction parallel to column axis; **c** the CJBs in the case between plane strain and plane stress; **d** the CJBs in the case of plane strain

of the sample, while there are many newly formed cracks caused by high stresses occurring in the right part of the sample. At the load Point F, the fracture zones at the middle part of the sample are connected, and the rest columns get broken more seriously. Compared with the lateral pressure of 0 MPa, the high lateral pressures can effectively restrain the fracturing of the vertical joints and improve the bearing capacity of specimen. Besides, as presented in Fig. 10f, the AE rate shows two peaks. The first peak is mainly because of the damage of vertical joints as well as some columns, and the second peak with more AE events results from the fracture of the columns.

(3) For the  $6 \text{ m} \times 3 \text{ m}$  model subjected to the lateral pressure of 0 MPa.

Figure 11a and b shows the stress–strain relationship and AE curve of  $6 \text{ m} \times 3 \text{ m}$  model under the lateral pressure of 0 MPa. Figure 11c and d shows the minor principal stress contours at the Points C and F of the stress–strain relationship. We can see that at the Point A, the obvious stress risers form in the middle of the specimen, where several vertical joints show the potential of cracking. With the load increased to the Point B, the vertical joints at the center of the sample get cracked. Meanwhile, the concentrated stresses mainly appear at the columns near these cracked joints. At the load Point C, many cracks form and expend at the center of several columns. After the load drops to the Point D, some cracks generate at the lower left and right parts of the model. After the load reaches the Point F, the inverted V-shaped fracture zone happens at the center of the specimen. Figure 11b indicates that the AE rate shows the multi-peak trend. The first AE peak is mainly because of the crack of the vertical joints, while the other AE peaks result from the rupture of columns and joints.

(4) For the  $6 \text{ m} \times 3 \text{ m}$  model subjected to the lateral pressure is 6 MPa.

Figure 11e and f depicts the stress–strain relationship and AE curve of  $6 \text{ m} \times 3 \text{ m}$  model under the lateral pressure of 6 MPa. Figure 11g and h shows the minor principal stress contours at the Points C and F of the stress–strain relationship. It can be seen that at the load Point A, relatively high stresses concentrate at the vertical joints in the middle of the model. With the loading increasing to the Point B, the

concentrated stresses occur at several columns at the center of the sample, forming an inverted V-shaped region. At the load Point C, more columns show significant stress concentrations in the middle of the specimen. After the load falls to the Point F, an obvious inverted V-shaped fracture zone appears in the middle of the specimen, which then gets damaged severely. Compared with the lateral pressure of 0 MPa, the high lateral pressures can apparently inhibit the cracking of vertical joints. Moreover, as depicted in Fig. 11f, the AE rate has a clear single-peak distribution, and the peak value is mainly because of the damage and failure at the middle of the model.

### 3.2.2 Along the Direction II Perpendicular to the Column Axis

(1) For the  $1.5 \text{ m} \times 3 \text{ m}$  model subjected to the lateral pressure of 0 MPa.

Figure 12a and b shows the stress–strain relationship and AE curve of  $1.5 \text{ m} \times 3 \text{ m}$  model under the lateral pressure of 0 MPa. Figure 12c and d shows the minor principal stress contours at the Points C and F of the stress–strain relationship. At the load Point A, the obvious stress risers form at the vertical joints of the model. With the stress increasing to the Point B, the vertical joints near the left and right boundaries of the model are cracked, while in the middle of the sample, the vertical joints are not damaged. At the load Point C, majority of the vertical joints are damaged. Simultaneously, the concentrated stresses at the oblique joints are obvious in the middle upper, lower left and lower right areas of the model. With the load decreasing to the Point D, numerous cracks initiate and propagate near the oblique joints within the inverted V-shaped high-stress region. For the Point F, the previously broken columns get damaged more seriously, and there are no obvious stress concentrations inside the specimen. As presented in Fig. 12b, the AE rate shows the double-peak distribution. The first AE peak is because of the fracturing of vertical joints, and the second AE peak results from the rupture of columns.

(2) For the  $1.5 \text{ m} \times 3 \text{ m}$  model subjected to the lateral pressure of 6 MPa.

Figure 12e and f displays the stress–strain relationship and AE curve of  $1.5 \text{ m} \times 3 \text{ m}$  model under the lateral pressure of 6 MPa. Figure 12g and h shows the minor principal stress contours at the Points C and F of the stress–strain relationship. At the load Point A, there are weak stress concentrations at the vertical joints in the left and right parts of the model. With the load increasing to the Point B, the stresses in these parts are intensified. After the load comes

**Table 3** Parameter values and calculation condition settings for numerical test on CJBs with transverse joints

Parameter	values and settings
Lateral pressure	0 MPa, 2 MPa, 4 MPa, 6 MPa, 8 MPa
Model size	1.5 m×3 m, 3 m×3 m, 6 m×3 m
Column dip angle $\beta$	0°, 15°, 30°, 45°, 60°, 75°, 90°
Heterogeneity index	5
Column diameter	20 cm
Elastic modulus of columnar joint	3.75 GPa, 7.5 GPa, 15 GPa, 22.5 GPa, 30 GPa
Residual strength coefficient of columnar joint	1
The ratio of shift distance of the secondary joint set (%)	The case without secondary joint set and the case with secondary joint set (the distance ratio 50% of the secondary joint set)
Residual strength coefficient of rock	0.1, 0.5, 0.75, 1
Model boundary	The case of plane strain and the case between plane stress and plane strain

**Table 4** Mechanical parameters of rock and joint in CJBs with transverse joints

Material type	Heterogeneity index	Elastic modulus (GPa)	Uniaxial compressive strength (MPa)	Poisson's ratio	Friction angle (°)	Residual strength coefficient
Basalt	5	60	120	0.2	56.15	0.1, 0.5, 0.75, 1
Joint	5	3.75, 7.5, 15, 22.5, 30	30	0.25	36	1

to the Point C, the vertical joints in the left and right areas of the model get ruptured. After the load drops to the Point D, the vertical joints at the middle upper, lower left and lower right parts of the sample are cracked. Meanwhile, the high stresses concentrate near the oblique joints. For the load Point E, the fractures are intensified near the oblique joints and the concentrated stresses are obvious. When the load researched the Point F, the previously cracked columns are broken more severely, and the inverted V-shaped fracture zone occur inside the specimen. Compared with the lateral pressure of 0 MPa, the high lateral pressure can restrain the cracking of vertical joints to a certain degree. In addition, as shown in Fig. 12f, the AE rate shows the single-peak distribution. The AE peak is mainly caused by the rupture of vertical and oblique joints and columns.

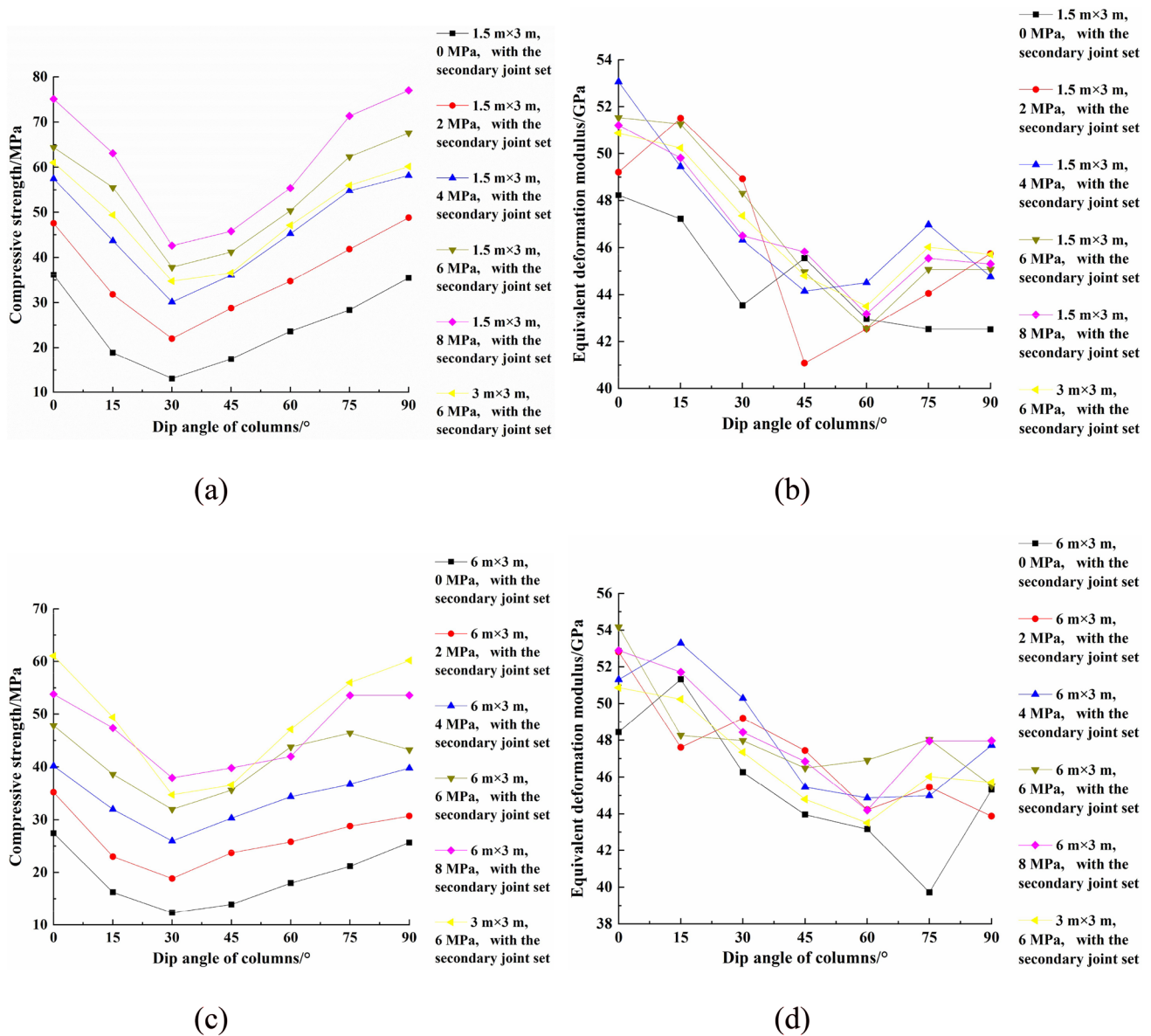
- (3) For the 6 m×3 m model subjected to the lateral pressure of 0 MPa.

Figure 13a and b shows the stress–strain relationship and AE curve of 6 m×3 m model under the lateral pressure of 0 MPa. Figure 13c and d shows the minor principal stress contours at the Points C and E of the stress–strain relationship. We can see that at the load Point A, there is an obvious stress-concentrated area at the middle of the sample, where several vertical joints are cracked. With the load increases to the Point B, there are more vertical joints cracked at the middle of the sample, and the other vertical joints near them

show significant stress concentration. At the load Point C, the cracks at the middle continuously extend to the top and bottom of the sample. There are approximately three X-shaped regions occurring in the sample. Additionally, at the middle of the specimen, new cracks form at some columns. When the load falls to the Point D, the cracks at the upper zone of the sample develop towards the top. Simultaneously, the obvious stress risers exist in the local zones near the top of the sample. At the Point F, there are more columns fractured in the upper part of the model. As depicted in Fig. 13b, the AE rate shows the double-peak distribution. The first AE peak is because of the fracturing of vertical joints, and the second AE peak results from the damage of vertical and oblique joints and the columns.

- (4) For the 6 m×3 m model subjected to the lateral pressure of 6 MPa.

Figure 13e and f depicts the stress–strain relationship and AE curve of 6 m×3 m model under the lateral pressure of 6 MPa. Figure 13g and h shows the minor principal stress contours at the Points C and E of the stress–strain relationship. We can see that at the load Point A, there is an inverted V-shaped high-stress region in the middle of the specimen, where stress concentrations appears obviously at the vertical joints. With the load increase to the Point B, the vertical joints with the significant stress concentrations are cracked, and the other vertical joints nearby therefore show stress



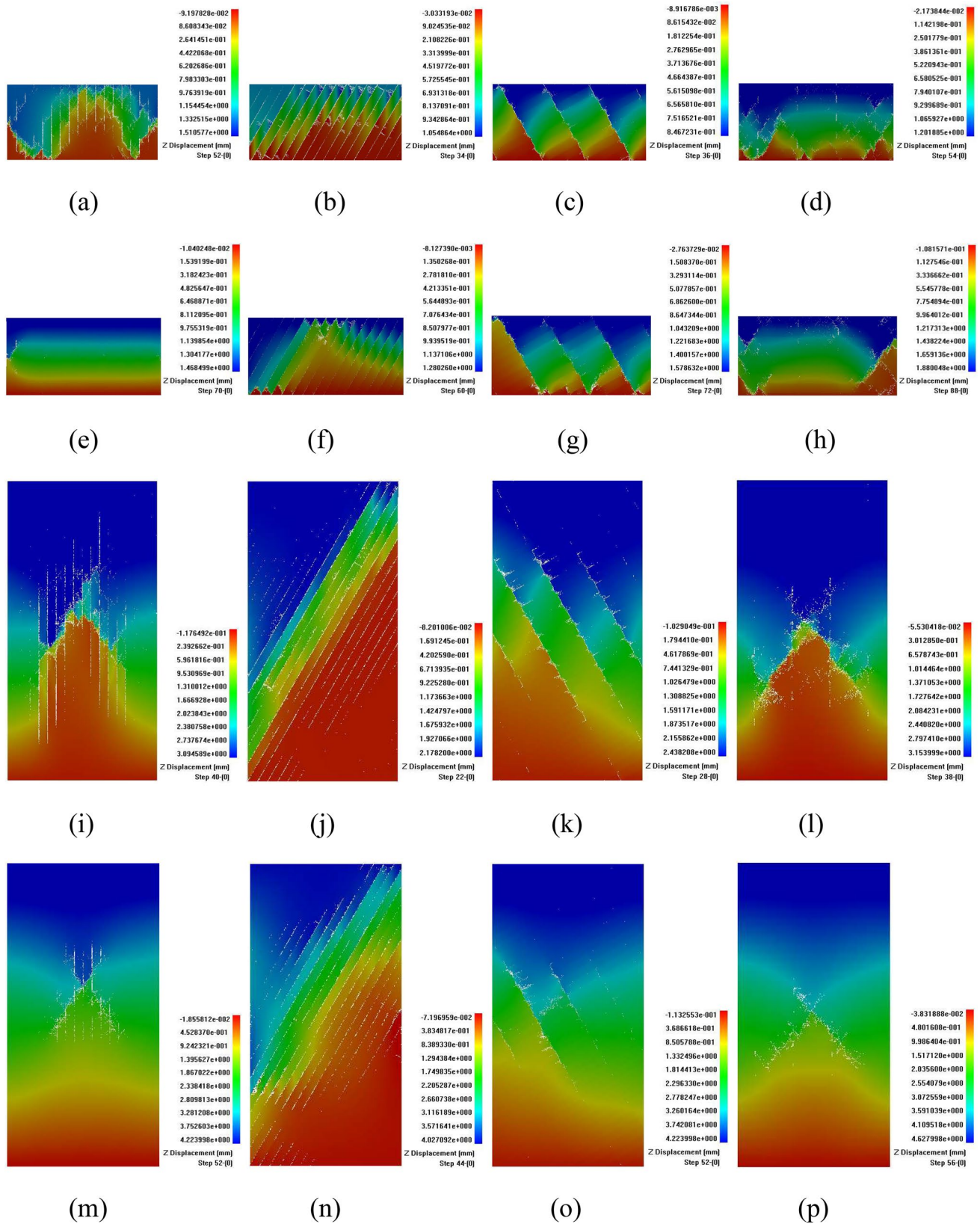
**Fig. 8** a and b The CSs and EDMs of the 1.5 m x 3 m and 3 m x 3 m samples under different lateral pressures; c and d the CSs and EDMs of the 3 m x 3 m and 6 m x 3 m samples under different lateral pressures

concentrations. At the load Point C, numerous cracks initiate near the oblique joints in the middle of the model. After the load falls to the Point D, the distinct inverted V-shaped region is formed in the middle, where the newly formed cracks expend. At the Points E and F, the cracks further propagate within the inverted V-shaped region. Compared with the lateral pressure of 0 MPa, the high confining pressures can inhibit the cracking of vertical and oblique joints and improve the bearing capacity of specimen to a certain extent.

### 3.2.3 Along the Direction Parallel to the Column Axis

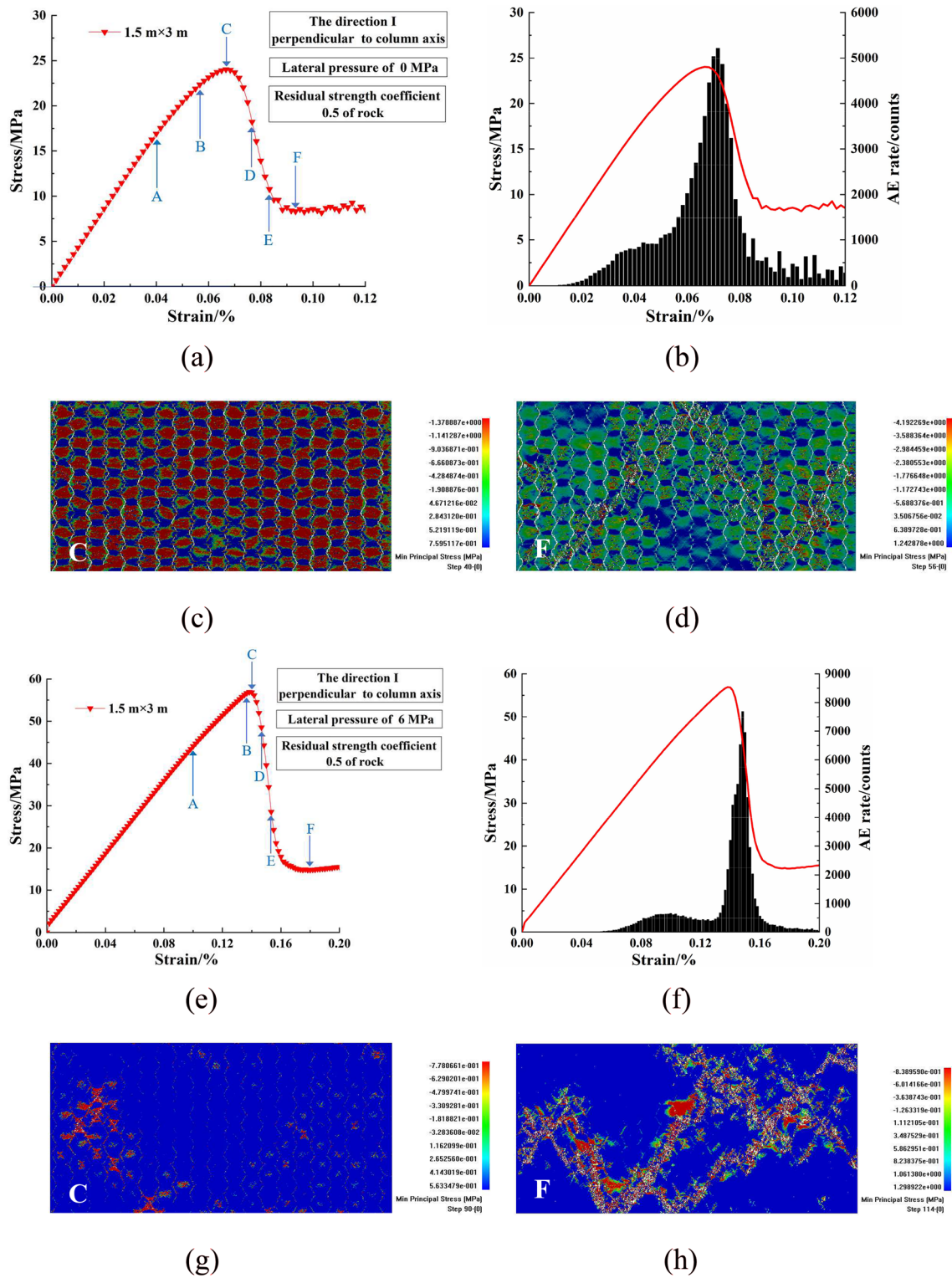
- (1) For the 1.5 m x 3 m and  $\beta = 45^\circ$  model subjected to the lateral pressure of 0 MPa.

Figure 14a and b shows the stress–strain relationship and AE curve of 1.5 m x 3 m model with the transverse joints for  $\beta = 45^\circ$ . Figure 14c and d shows the minor principal stress contours at the Points C and F of the stress–strain relationship. It is clear that at the load Point A, the columnar joints and transverse joints in the model

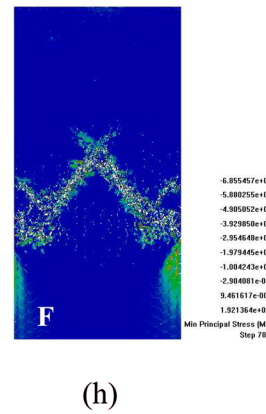
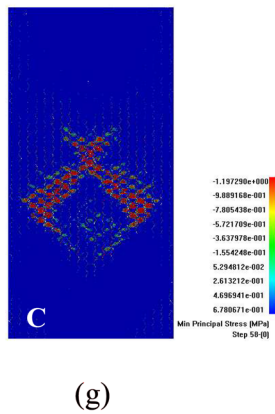
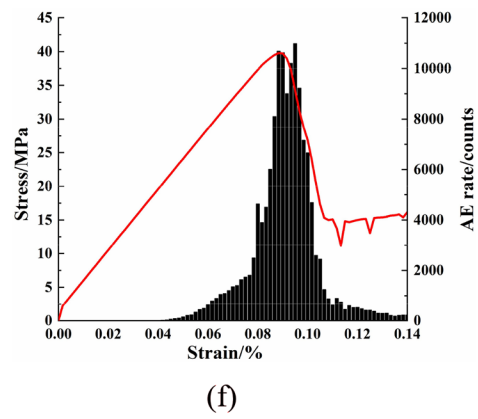
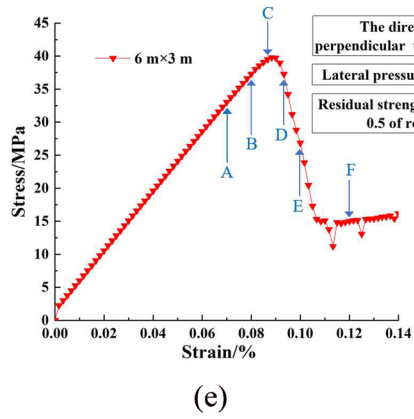
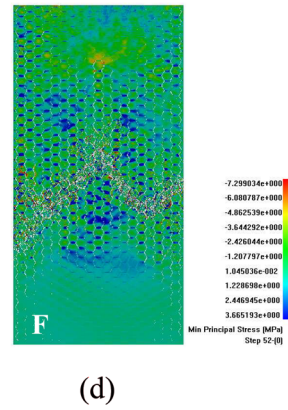
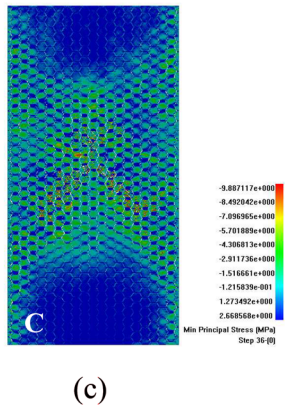
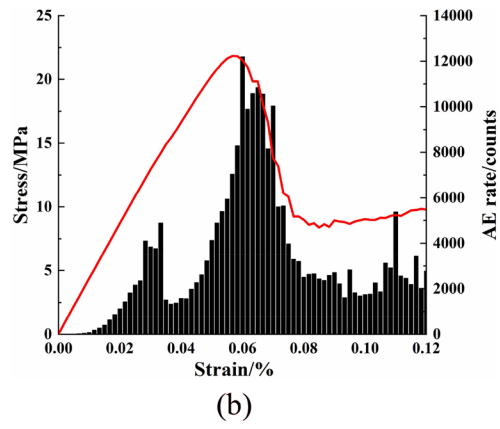
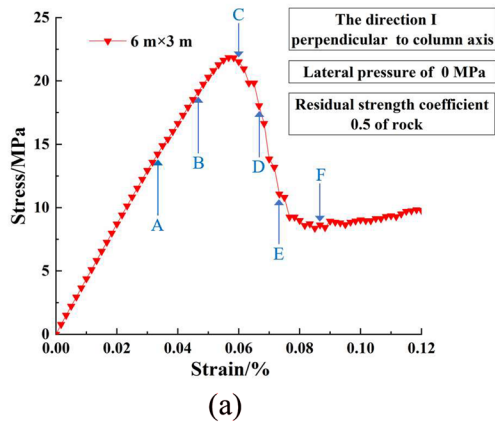


**Fig. 9** The z-direction displacement contours when  $\beta=0^\circ$ ,  $30^\circ$ ,  $60^\circ$  and  $90^\circ$ : **a–d** the 1.5 m × 3 m samples with transverse joints when the lateral pressure = 0 MPa; **e–h** the 1.5 m × 3 m samples when the

lateral pressure = 4 MPa; **i–l** the 6 m × 3 m samples when the lateral pressure = 0 MPa; **m–p** the 6 m × 3 m CJBs when the lateral pressure = 4 MPa



**Fig. 10** Progressive fracture process and failure pattern of the 1.5 m x 3 m samples along the direction I perpendicular to column axis: **a** and **b** the stress–strain curve and AE rate under the lateral pressure of 0 MPa; **c** and **d** the minimum principal stress contours corresponding to Points C and F of the stress–strain curve; **e** and **f** the stress–strain curve and AE rate under the lateral pressure of 6 MPa; **g** and **h** the minimum principal stress contours corresponding to Points C and F of the stress–strain curve



◀**Fig. 11** Progressive fracture process and failure pattern of the 6 m × 3 m samples along the direction I perpendicular to column axis: **a** and **b** the stress–strain curve and AE rate under the lateral pressure of 0 MPa; **c** and **d** the minimum principal stress contours corresponding to Points C and F of the stress–strain curve; **e** and **f** the stress–strain curve and AE rate under the lateral pressure of 6 MPa; **g** and **h** the minimum principal stress contours corresponding to Points C and F of the stress–strain curve

show significant stress risers. With the loading increasing to the Point C, the columnar joints inside the sample show obvious slip cracking. At the load Point D, some transverse joints get cracked, and the high stresses appear at the edges of a few columns at the lower left and upper right areas of the sample. After the load comes to the Point E, more cracks generate and propagate at the edges of the columns. Simultaneously, the high stresses concentrate at the crack tips, resulting in that the other transverse joints inside the sample are also cracked. At the load Point F, the cracks further propagate at the lower left and upper right parts of the model. Besides, as presented in Fig. 14b, the AE rate shows the double-peak distribution. The first AE peak is mainly because of the slipping of columnar joints, and the second AE peak is due to the failure of transverse joints and columns.

- (2) For the 1.5 m × 3 m and  $\beta = 45^\circ$  model subjected to the lateral pressure of 6 MPa.

Figure 14e and f displays the stress–strain relationship and AE curve of 1.5 m × 3 m model with the transverse joints for  $\beta = 45^\circ$ . Figure 14g and h shows the minor principal stress contours at the Points C and E of the stress–strain relationship. At the load Points A and B, the columnar joints in the model show weak stress risers. With the loading rising to the Point C, the concentrated stresses at the columnar joints increase. At the load Point D, there are many cracks initiating and propagating at the middle upper area of the model. Simultaneously, a strip region forms, where the high stresses concentrate at the edges of several columns. After the stress drops to the Point E, the cracks continue to expend within the strip region. At the Point F, more cracks initiate and propagate near the top of the model. Meanwhile, a strip fractured zone appears near the right boundary of the specimen, and the fractures get intensified. Compared with the lateral pressure of 0 MPa, the high lateral pressures can effectively restrain the slipping of columnar joints. Additionally, as shown in Fig. 14f, the AE rate show the multi-peak distribution. The first AE peak is mainly because of the damage of columnar joints, and the other AE peaks result from the rupture of columns.

- (3) For the 6 m × 3 m and  $\beta = 45^\circ$  model subjected to the lateral pressure of 0 MPa.

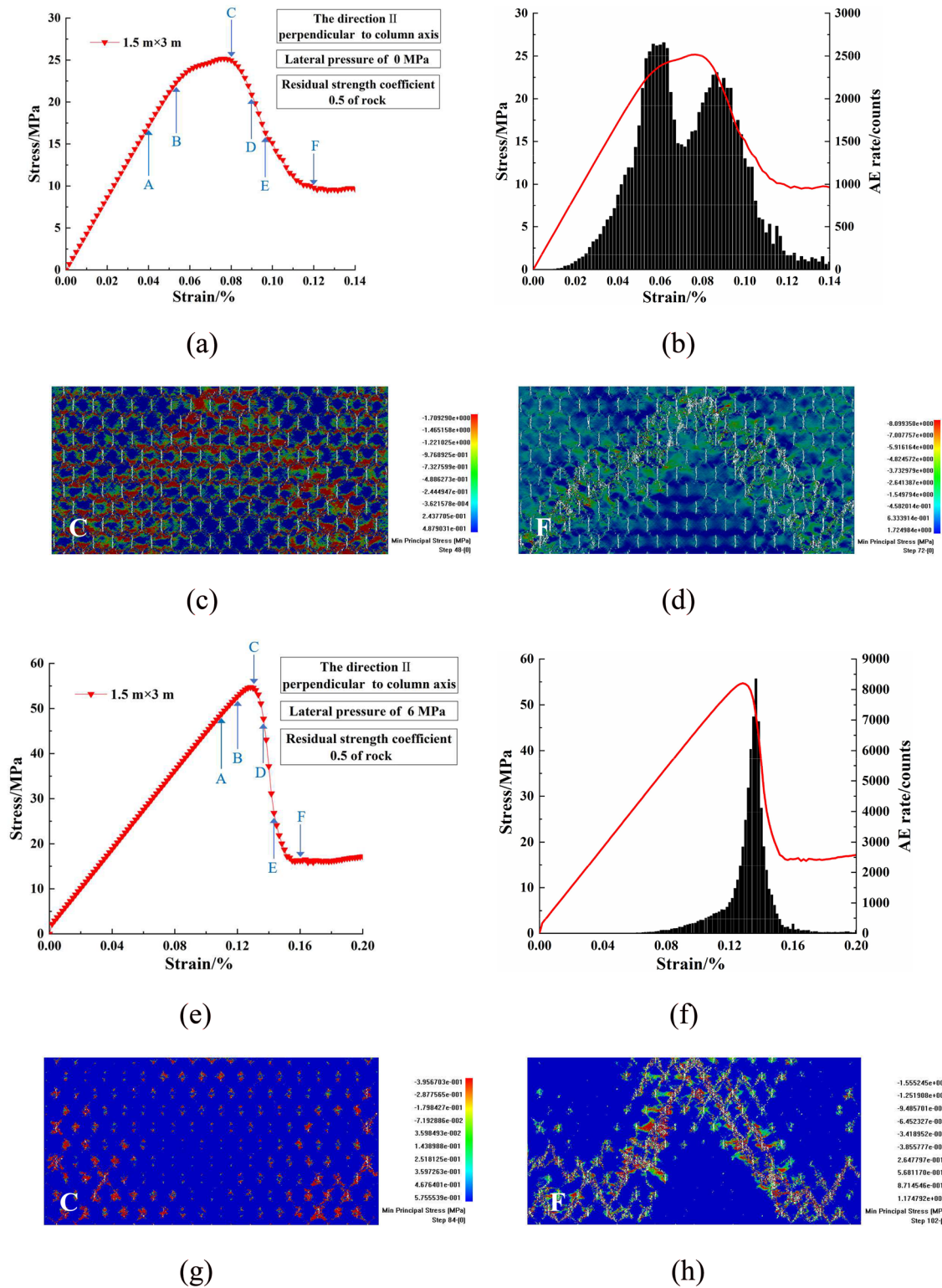
Figure 15a and b shows the stress–strain relationship and AE curve of 6 m × 3 m model with the transverse joints for  $\beta = 45^\circ$ . Figure 15c and d shows the minor principal stress contours at the Points B and E of the stress–strain relationship. We can see that at the load Points A and B, there is an obvious stress-concentrated region in the middle of the sample, where some columnar joints slip. With the stress decreasing to the Point C, the slipping of the columnar joints further develops. Simultaneously, high stress values appear at the edges of a few columns, and the transverse joints get cracked gradually. At the load Point E, the fracturing of the columns get intensified at the center of the sample. Moreover, Fig. 15b illustrates the AE rate shows the double-peak distribution. The first peak is due to the slipping of columnar joints, and the second peak results from the cracking of transverse joints and columns.

- (4) For the 6 m × 3 m and  $\beta = 45^\circ$  model subjected to the lateral pressure of 6 MPa.

Figure 15e and f depicts the stress–strain relationship and AE curve of 6 m × 3 m model with the transverse joints for  $\beta = 45^\circ$ . Figure 15g and h shows the minor principal stress contours at the Points B and E of the stress–strain relationship. At the load Points A and B, the distinct stress risers occur in the columnar joints in the middle of the model. With the stress increasing to the peak Point C, high stresses concentrate at some columns at the left side of the model. At the load Point D, a strip region with obvious stress risers forms at the left side, and a local region with weak stress concentrations occurs at the right side. After the stress drops to the Point E, there are two strip fractured regions near the left boundary of the sample. At the Point F, the strip fractured regions continue to develop towards the right boundary. Compared with the lateral pressure of 0 MPa, the high lateral pressures can apparently inhibit the slipping of columnar joints. In addition, as presented in Fig. 15f, the AE rate shows the multi-peak distribution. The first AE peak is caused by the damage of columnar joints, and the other AE peaks are mainly due to the fracture of columns.

### 3.3 Influence of Transverse Joints on Anisotropy and Shape Effect of CJBs

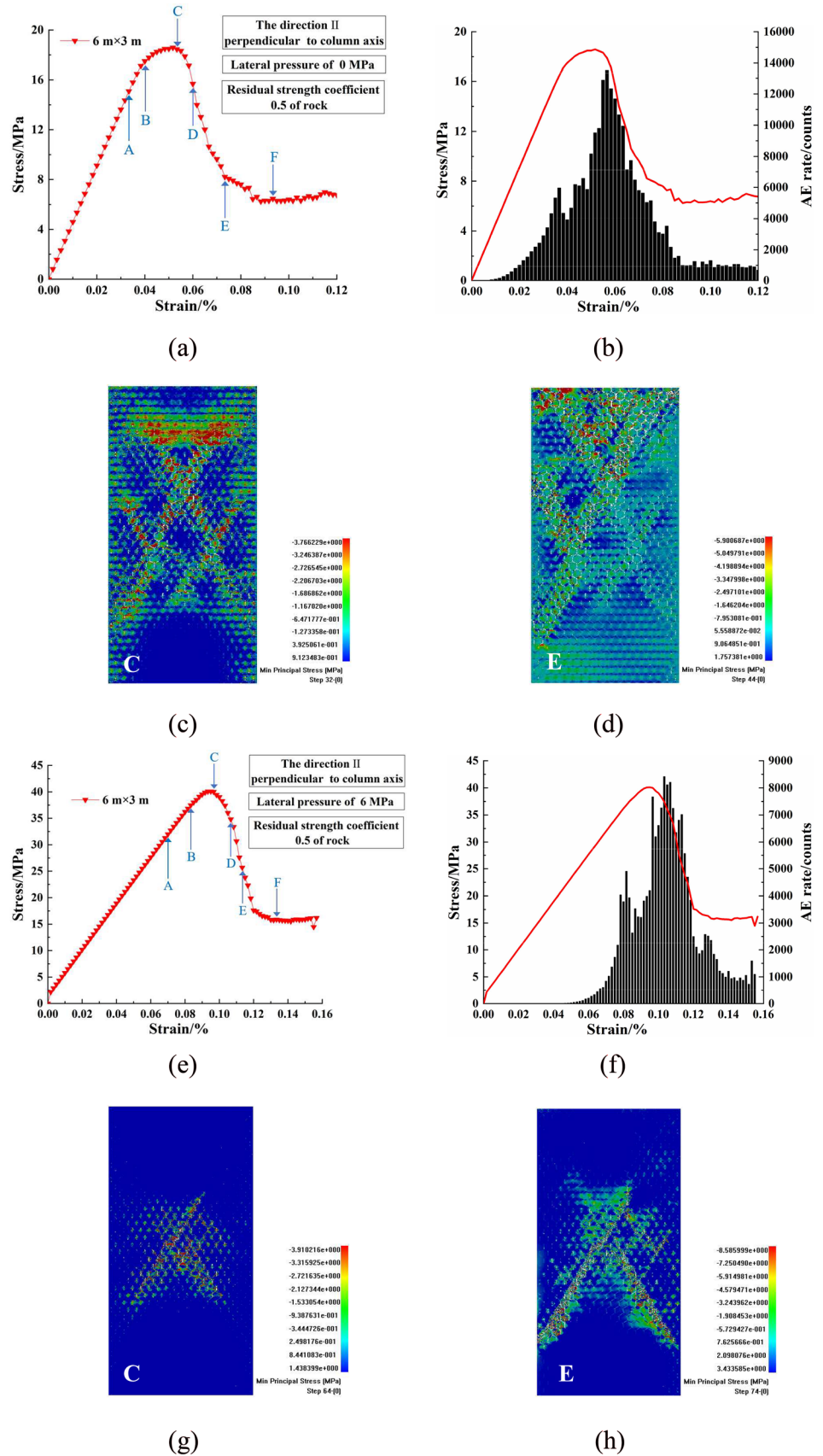
Figure 16a demonstrates that for the 1.5 m × 3 m specimen subjected to the lateral pressure of 0 MPa, the CSs of the samples with transverse joints are lower than the specimens without transverse joints at the dip angles of  $0^\circ$ ,  $60^\circ$  and  $75^\circ$ . Under the lateral pressure of 6 MPa, the CS of the sample with transverse joints is lower than the sample without transverse joints at the dip angle of  $0^\circ$ . At the other dip angles, the transverse joints have little effect on the CS. For  $\beta = 60^\circ$  and  $75^\circ$ , the existence of lateral pressure will weaken the effect

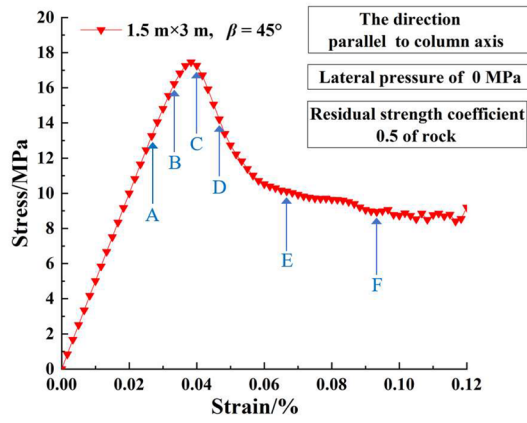


**Fig. 12** Progressive fracture process and failure pattern of the 1.5 m  $\times$  3 m samples along the direction II perpendicular to column axis: **a** and **b** the stress–strain curve and AE rate under the lateral pressure of 0 MPa; **c** and **d** the minimum principal stress contours

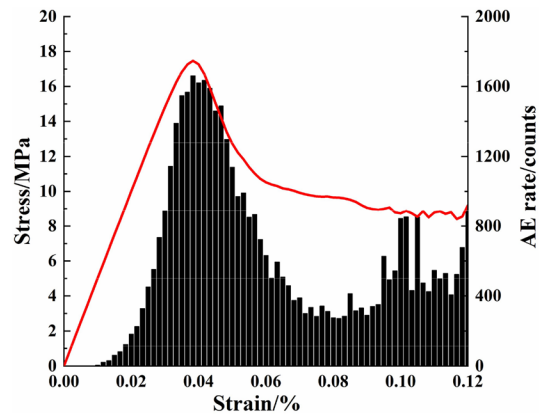
corresponding to Points C and F of the stress–strain curve; **e** and **f** the stress–strain curve and AE rate under the lateral pressure of 6 MPa; **g** and **h** the minimum principal stress contours corresponding to Points C and F of the stress–strain curve

**Fig. 13** Progressive fracture process and failure pattern of the  $6\text{ m} \times 3\text{ m}$  samples along the direction II perpendicular to column axis: **a** and **b** the stress-strain curve and AE rate under the lateral pressure of 0 MPa; **c** and **d** the minimum principal stress contours corresponding to Points C and E of the stress-strain curve; **e** and **f** the stress-strain curve and AE rate under the lateral pressure of 6 MPa; **g** and **h** the minimum principal stress contours corresponding to Points C and E of the stress-strain curve

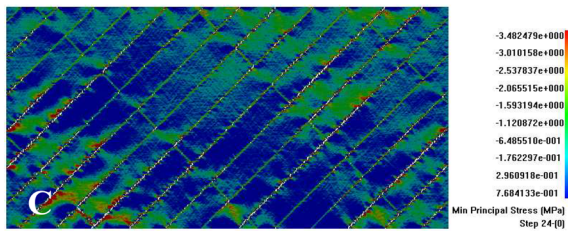




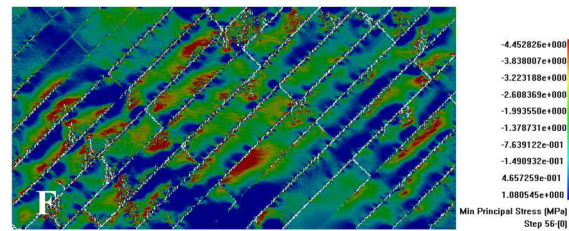
(a)



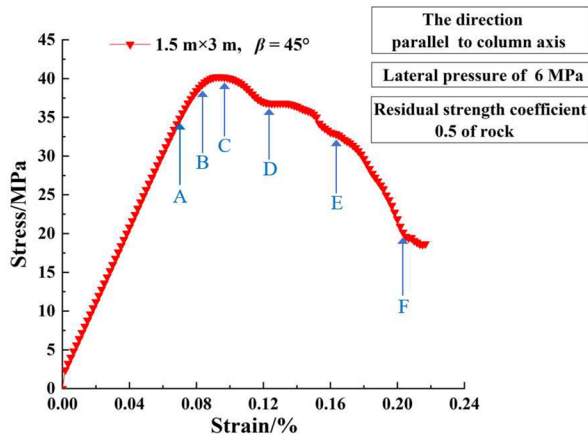
(b)



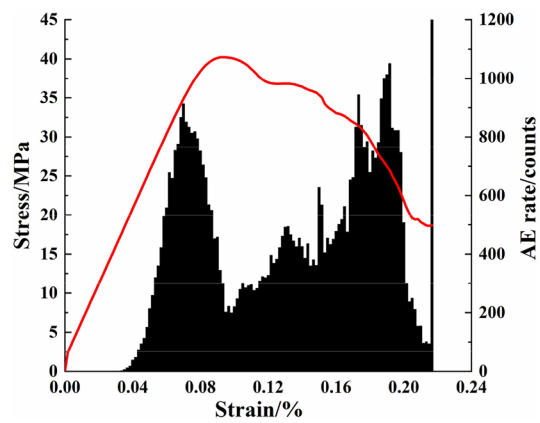
(c)



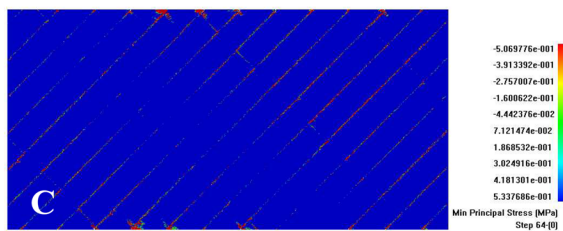
(d)



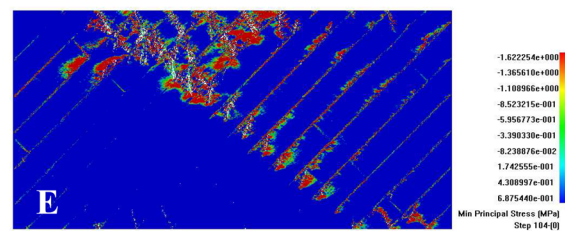
(e)



(f)



(g)



(h)

**Fig. 14** Progressive fracture process and failure pattern of the  $1.5 \text{ m} \times 3 \text{ m}$  samples along the direction parallel to column axis: **a** and **b** the stress–strain curve and AE rate under the lateral pressure of 0 MPa; **c** and **d** the minimum principal stress contours corresponding to Points C and F of the stress–strain curve; **e** and **f** the stress–strain curve and AE rate under the lateral pressure of 6 MPa; **g** and **h** the minimum principal stress contours corresponding to Points C and E of the stress–strain curve

of transverse joints on the CSs of the samples. Figure 16b indicates that for the  $1.5 \text{ m} \times 3 \text{ m}$  sample, the EDMs of the specimens with transverse joints are lower than the specimens without transverse joints at the dip angles of  $0^\circ$ – $30^\circ$  and  $75^\circ$ – $90^\circ$  under the lateral pressure of 0 MPa. Under the lateral pressure of 6 MPa, the EDMs of the specimens with transverse joints are lower than the specimens without transverse joints at the dip angles of  $0^\circ$  and  $75^\circ$ – $90^\circ$ . At the other dip angles, the influence of transverse joints on the EDMs of the specimens is very small.

As presented in Fig. 16c, for the  $6 \text{ m} \times 3 \text{ m}$  specimen, the CSs of the specimens with transverse joints are lower than the specimens without transverse joints at the dip angles of  $60^\circ$  and  $75^\circ$  under the lateral pressure of 0 MPa. Under the lateral pressure of 6 MPa, the CSs of the samples containing transverse joints are lower than the samples without transverse joints at the dip angles of  $15^\circ$  and  $75^\circ$ . At the other dip angles, the transverse joints have little effect on the CS. For  $\beta = 60^\circ$ , the existence of lateral pressure will weaken the effect of transverse joints on the CSs of the specimens. As depicted in Fig. 16d, for the  $6 \text{ m} \times 3 \text{ m}$  specimen, the EDMs of the specimens with transverse joints are lower than the specimens without transverse joints at the dip angles of  $0^\circ$ ,  $45^\circ$  and  $75^\circ$  under the lateral pressure of 0 MPa. Under the lateral pressure of 6 MPa, the EDMs of the samples containing transverse joints are lower than the specimens without transverse joints at the dip angles of  $15^\circ$ – $30^\circ$  and  $75^\circ$ – $90^\circ$ .

According to Fig. 16e, the influence of specimen shape on CS is more obvious than transverse joints if the lateral pressure = 6 MPa and  $\beta = 0^\circ$ – $90^\circ$ . Especially, at the dip angles of  $0^\circ$ – $15^\circ$  and  $75^\circ$ – $90^\circ$ , the specimen shape has a great influence on the model CSs. Figure 16f indicates that the influence of specimen shape on EDM is more obvious than transverse joints if the lateral pressure = 6 MPa and  $\beta = 0^\circ$ – $90^\circ$ . Especially, at the dip angles of  $15^\circ$  and  $60^\circ$ – $75^\circ$ , the specimen shape has relatively obvious influence on the EDMs of the specimens.

As presented in Fig. 17a, for the  $6 \text{ m} \times 3 \text{ m}$  and  $\beta = 60^\circ$  specimen without transverse joints, an inverted V-shaped fractured region appears at the middle under the lateral pressure of 0 MPa. As displayed in Fig. 17b, an X-shaped fractured region is formed at the left side, and there is a strip stress-concentrated region at the right side under the lateral pressure of 6 MPa. Figure 17c illustrates that for the  $6 \text{ m} \times 3 \text{ m}$  and  $\beta = 60^\circ$  specimen with transverse joints, the

transverse joints in the middle of the model get damaged, and the obvious concentrated stresses occur near the columns when the lateral pressure = 0 MPa; As displayed in Fig. 17d, in the middle of the specimen, there are transverse joints showing the shear-fractured mode, and the breakages are connected. Meanwhile, the cracks initiate and develop near the columns when the lateral pressure = 6 MPa.

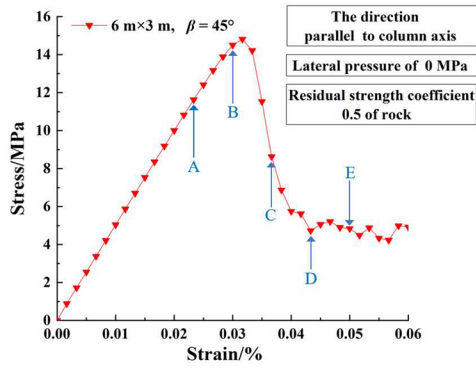
### 3.4 Influence of Elastic Modulus of Joints on Shape Effect of CJBs

Figure 18 illustrates that for the  $1.5 \text{ m} \times 3 \text{ m}$ ,  $3 \text{ m} \times 3 \text{ m}$  and  $6 \text{ m} \times 3 \text{ m}$  specimens, the CS grows as the elastic modulus of joints increases. In addition, the CS of the  $1.5 \text{ m} \times 3 \text{ m}$  specimen is the highest, and the CS of the  $6 \text{ m} \times 3 \text{ m}$  specimen is the lowest. As depicted in Fig. 18, for the  $1.5 \text{ m} \times 3 \text{ m}$ ,  $3 \text{ m} \times 3 \text{ m}$  and  $6 \text{ m} \times 3 \text{ m}$  specimens, as the elastic modulus of joints increases, the EDMs of the specimens firstly increase quickly and then slowly. For the  $1.5 \text{ m} \times 3 \text{ m}$  specimen, if the elastic modulus of joints exceeds 15 GPa, the change of the EDM will be slow. For the  $3 \text{ m} \times 3 \text{ m}$  and  $6 \text{ m} \times 3 \text{ m}$  specimens, if the elastic modulus of joints becomes greater than 7.5 GPa, the change of the EDM will also be very gentle.

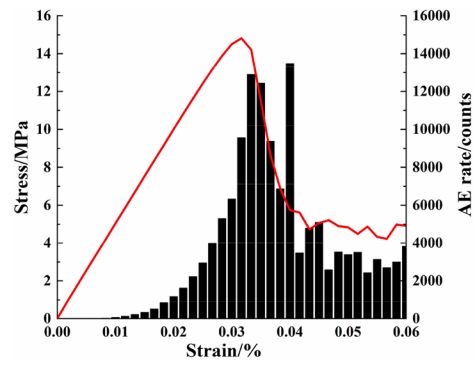
### 3.5 Influence of Residual Strength Coefficient of Rock on Anisotropy and Shape Effect of CJBs

Figure 19a demonstrates that for the  $1.5 \text{ m} \times 3 \text{ m}$  sample with transverse joints, the residual strength coefficient of rocks has a great influence on the CS at the dip angles of  $0^\circ$  and  $75^\circ$ – $90^\circ$  when the lateral pressure = 6 MPa. At the other dip angles, the residual strength coefficient shows little influence on the CS. As the residual strength coefficient of rocks rises, the CS of the specimen increases obviously at the dip angles of  $0^\circ$  and  $75^\circ$ – $90^\circ$ . At the other dip angles, the change of the residual strength coefficient of rocks almost shows no significant influence on the CS. According to Fig. 19b, for the  $1.5 \text{ m} \times 3 \text{ m}$  specimen with transverse joints, if the residual strength coefficient of rock equals 0.1 or 0.5, the change range of the EDMs will be relatively small as the dip angle increases, and the minimum values of the EDMs appear when the dip angle =  $60^\circ$  and the lateral pressure = 6 MPa. If the residual strength coefficient of rock equals 0.75 or 1, the change range of the EDMs will be relatively large as the dip angle increases, and the minimum values of the EDMs appear when the dip angle =  $30^\circ$ .

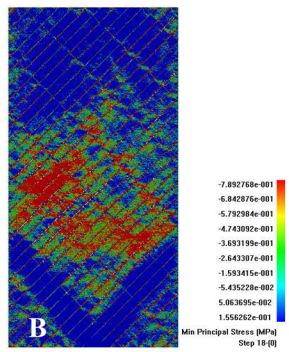
As shown in Fig. 19c, for the  $6 \text{ m} \times 3 \text{ m}$  specimen with transverse joints, the residual strength coefficient of rock has a great influence on the CS at the dip angles of  $0^\circ$  and  $60^\circ$ – $90^\circ$  when the lateral pressure = 6 MPa. At the other dip angles, the residual strength coefficient shows little influence on the CS. For the dip angles of  $0^\circ$  and  $60^\circ$ – $90^\circ$ , with the residual strength coefficient of rock increasing from 0.75 to



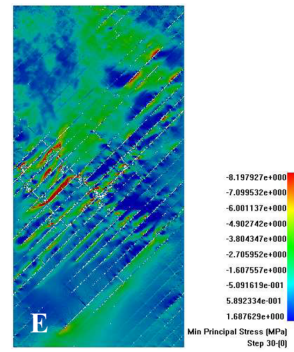
(a)



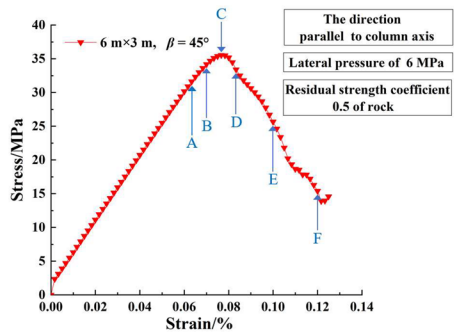
(b)



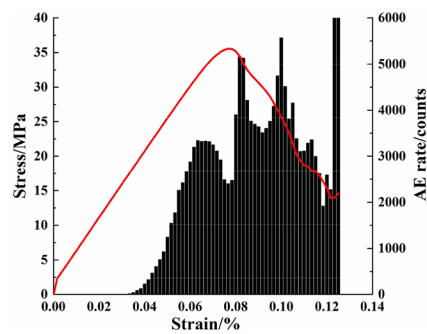
(c)



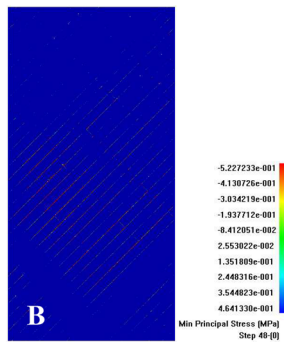
(d)



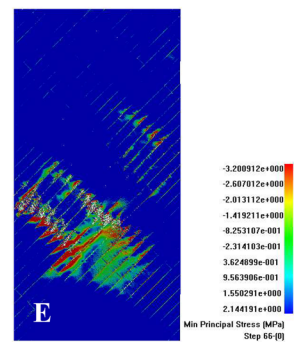
(e)



(f)



(g)



(h)

**Fig. 15** Progressive fracture process and failure pattern for the  $6\text{ m} \times 3\text{ m}$  samples along the direction parallel to column axis: **a** and **b** the stress–strain curve and AE rate under the lateral pressure of 0 MPa; **c** and **d** the minimum principal stress contours corresponding to Points B and E of the stress–strain curve; **e** and **f** the stress–strain curve and AE rate under the lateral pressure of 6 MPa; **g** and **h** the minimum principal stress contours corresponding to Points B and E of the stress–strain curve

1, the CS grows up obviously. At the other dip angles, the variation of the residual strength coefficient of rocks shows no significant influence on the CS. Figure 19d illustrates that for the  $6\text{ m} \times 3\text{ m}$  specimen with transverse joints, if the residual strength coefficient of rocks is among 0.1–1, the EDMs of the specimens firstly decrease but then grow (or change) as the column dip angle increases under the lateral pressure of 6 MPa. When the residual strength coefficient of rock equals 0.1, the minimum values of the EDMs appear at the column dip angle of  $90^\circ$ . When the residual strength coefficients of rock are 0.5, 0.75 and 1, the minimum values of the EDMs appear at the column dip angle of  $60^\circ$ .

### 3.6 Influence of Model Boundary on Anisotropy and Shape Effect of CJBs

In Fig. 20a, the CSs of  $1.5\text{ m} \times 3\text{ m}$ ,  $3\text{ m} \times 3\text{ m}$  and  $6\text{ m} \times 3\text{ m}$  specimens with transverse joints and different model boundaries are compared under the lateral pressure of 6 MPa. When the case between plane stress and plane strain is considered, as the column dip angle increases, the CS of the samples basically decreases at the beginning and then changes gently. Clearly, when the column dip angle exceeds  $30^\circ$ , the CS changes slowly. When the case of plane strain is considered, the CS of the specimens changes in a U-shape form with the column dip angle increasing. The CS of the samples reaches the minimum when the column dip angle =  $30^\circ$ .

In Fig. 20b, the EDMs of  $1.5\text{ m} \times 3\text{ m}$ ,  $3\text{ m} \times 3\text{ m}$  and  $6\text{ m} \times 3\text{ m}$  specimens with transverse joints and different model boundaries are compared when the lateral pressure = 6 MPa. When the case between plane stress and plane strain is considered, the change range of the EDM of the  $1.5\text{ m} \times 3\text{ m}$  specimen is the largest, and the change range of the  $6\text{ m} \times 3\text{ m}$  specimen is the smallest as the column dip angle increases. The minimum EDMs of the  $1.5\text{ m} \times 3\text{ m}$  and  $6\text{ m} \times 3\text{ m}$  specimens appear at the dip angle of  $90^\circ$ . However, for the  $3\text{ m} \times 3\text{ m}$  specimens, it appears at the dip angle of  $75^\circ$ . When the case of plane strain is considered, the EDMs of  $1.5\text{ m} \times 3\text{ m}$ ,  $3\text{ m} \times 3\text{ m}$  and  $6\text{ m} \times 3\text{ m}$  samples basically decrease firstly and then grow with the column dip angle rising.

## 4 Discussion

### 4.1 Analysis of Shape Effect of CJBs with Transverse Joints

When the lateral pressure = 0 MPa, the gradual fracture process and failure mode of the  $1.5\text{ m} \times 3\text{ m}$  and  $\beta = 45^\circ$  sample with transverse joints along the direction parallel to the column axis can be concluded as follows: because of the continuous loading, the columnar joints inside the sample gradually get slipped and cracked. Then, some transverse joints are cracked, and new cracks generate and extend the edges of several columns at the lower left and upper right parts of the sample. Meanwhile, the other transverse joints inside the sample are cracked as well; with the load increasing, these cracks further propagate along the edges of columns.

When the lateral pressure = 6 MPa, the gradual fracture process and failure mode of the  $1.5\text{ m} \times 3\text{ m}$  and  $\beta = 45^\circ$  sample with transverse joints along the direction parallel to the column axis can be concluded as follows: because of the loading, there are cracks initiating and propagating near the middle upper part of the sample. Then, cracks extend along the edges of a few columns within the strip stress-concentrated region. With the load increasing, there are more cracks generating near the top of the model. Simultaneously, a strip fractured region appears at the right side of the model, and the fracturing get intensified.

When the lateral pressure = 0 MPa, the gradual fracture process and failure mode of the  $6\text{ m} \times 3\text{ m}$  and  $\beta = 45^\circ$  sample with transverse joints along the direction parallel to the column axis can be concluded as follows: at the beginning of loading, the columnar joints slip at the middle of the specimen. Then, the slipping of the columnar joints further develops, and obviously concentrated stresses appear along the edges of a few columns. Meanwhile, the transverse joints are cracked gradually. With the load increasing, the cracking of transverse joints further develops at the middle of the specimen, and the fracture of the columns are intensified.

When the lateral pressure = 6 MPa, the gradual fracture process and failure mode of the  $6\text{ m} \times 3\text{ m}$  and  $\beta = 45^\circ$  sample with transverse joints along the direction parallel to the column axis can be concluded as follows: at the beginning of loading, a strip stress-concentrated region forms at the middle left part of the model, and the local stress concentrations appear at the middle right part of the model. Furthermore, with the load growing, two strip fractured regions appear near the left boundary of the sample. Then, at the middle lower part of the specimen, the fractured zone further develops and the fracturing is intensified.

Lin et al. (2018) studied the shape effect of CJRMs with transverse joints under uniaxial compression by the

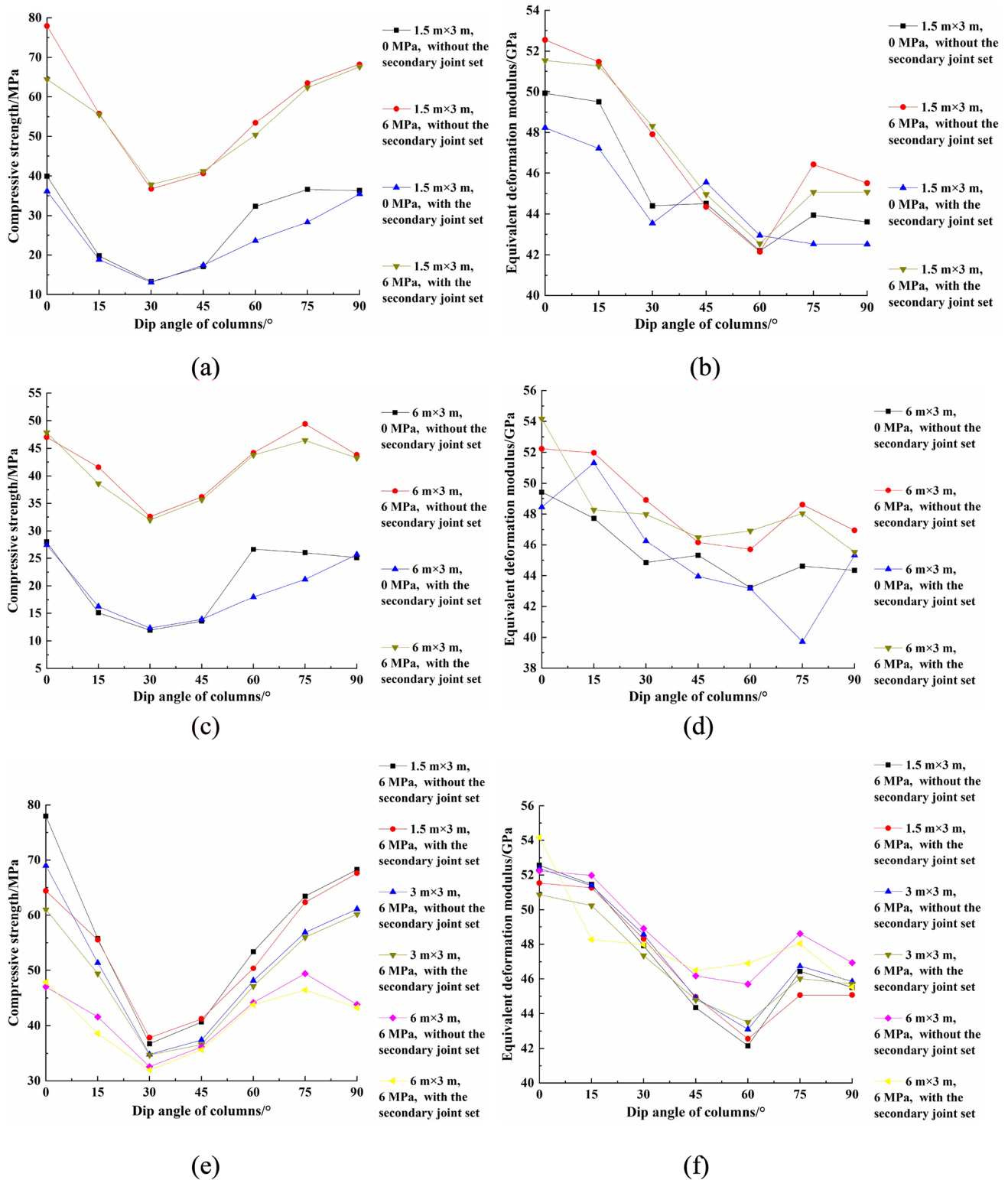


**Fig. 16** The CSs and EDMs: **a** and **b** the 1.5 m × 3 m samples without and with transverse joints; **c** and **d** the 6 m × 3 m samples without and with transverse joints; **e** and **f** the 1.5 m × 3 m, 3 m × 3 m and 6 m × 3 m samples without and with transverse joints

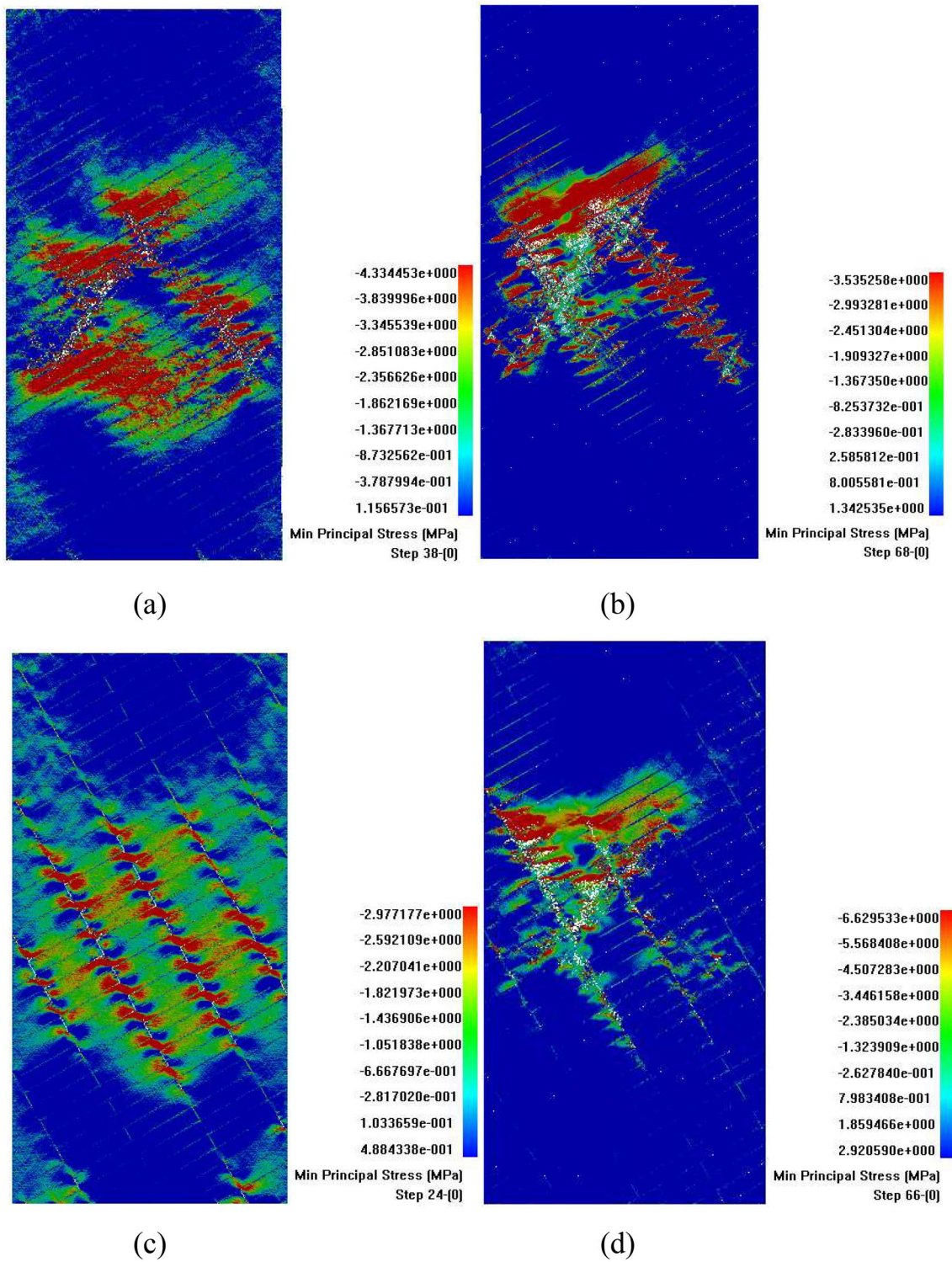
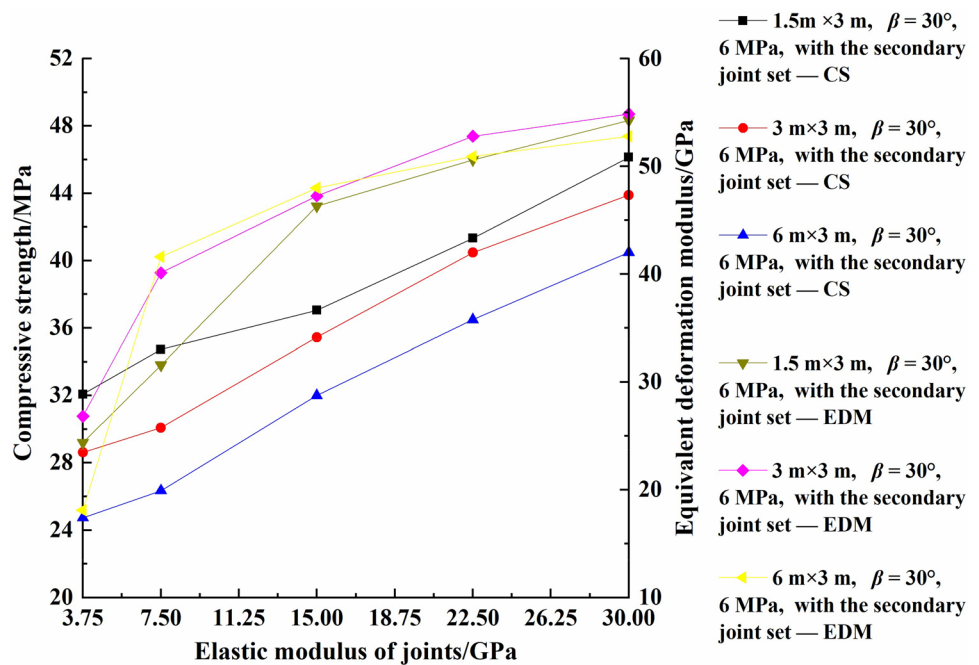


**Fig. 17** The minimum principal stress contours: **a** the 6 m×3 m sample without the secondary joint set when the lateral pressures=0 MPa and  $\beta=60^\circ$ ; **b** the 6 m×3 m sample without the secondary joint set when the lateral pressures=6 MPa and  $\beta=60^\circ$ ; **c** the 6 m×3 m sam-

ple with the secondary joint set when the lateral pressures=0 MPa and  $\beta=60^\circ$ ; **d** the 6 m×3 m sample with the secondary joint set when the lateral pressures=6 MPa and  $\beta=60^\circ$

**Fig. 18** The CSs and EDMs of the 1.5 m×3 m, 3 m×3 m and 6 m×3 m samples when the lateral pressure=6 MPa and  $\beta=30^\circ$  under different elastic moduli of joints



experimental tests and analyzed the strength anisotropy and fracture mode. But the progressive fracture process of their specimens was not presented, and the influence of confining pressure was not considered in their study. Xiao et al. (2015a, b) investigated the mechanical parameters and fracture mode of CJRMs subjected to uniaxial compression by the physical tests. But in their study, the cement paste was used to bond the columns to simulate the role of joints between the columns, which is different from the actual joints. Zhu et al. (2021) performed a group of physical tests to reveal the mechanical behaviors and deformation features of CJRMs subject to the three-dimensional stress. However, the influence of transverse joints and shape effect were not considered. Xia et al. (2020a, b) discussed the anisotropy and fracture mode of irregular CJRMs subjected to uniaxial compression using the 3D printing technology. But the stress field evolution process of the specimens was not captured. Huang et al. (2020) applied the 3D printing technology to make the molds, poured the irregular CJRMs, and investigated their nonlinear deformation behaviors under uniaxial compression. Nevertheless, the mechanical parameters of the column binder were different from the actual joints, which may change the failure mechanisms of the samples. Wang et al. (2016) studied the anisotropy and size effect of jointed rock masses by DEM. Their results showed that when the sample size is relatively small, the deformation modulus and UCS fluctuate greatly; with the sample size increasing, they will stabilize at a certain value. However, the influence of confining pressure was not considered in their study. Cui et al. (2015) discussed the influence of the structural effect, the distance ratio of joints, joint stiffness,

column irregularity on the EDM of specimens, but the shape effect was not further considered. Wu et al. (2019) studied the anisotropy of jointed rock masses subjected to confining pressure, but the shape effect needed to be further studied because of the mutual influence.

#### 4.2 Influence of Transverse Joints on Anisotropy and Shape Effect of CJBs

The strength characteristics of the 1.5 m×3 m sample along the direction parallel to the column axis are summarized as follows: under the lateral pressure of 0 MPa, the CSs of the samples containing transverse joints are lower than the samples without transverse joints at the dip angles of  $0^\circ$ ,  $60^\circ$  and  $75^\circ$ . At the other dip angles, the transverse joints have little effect on the CS. When the lateral pressure = 6 MPa, the CS of the sample containing transverse joints is lower than the sample without transverse joints at the dip angle of  $0^\circ$ . At the other dip angles, the transverse joints have little effect on the CS. For  $\beta=60^\circ$  and  $75^\circ$ , the existence of lateral pressure will weaken the effect of transverse joints on the CSs of the samples.

The strength characteristics of the 6 m×3 m sample along the direction parallel to the column axis are summarized as follows: under the lateral pressure of 0 MPa, the CSs of the samples containing transverse joints are lower than the samples without transverse joints at the dip angles of  $60^\circ$  and  $75^\circ$ . At the other dip angles, the transverse joints have little effect on the CS. When the lateral pressure = 6 MPa, the CS of the sample containing transverse joints is lower than the sample without transverse joints at the dip angles

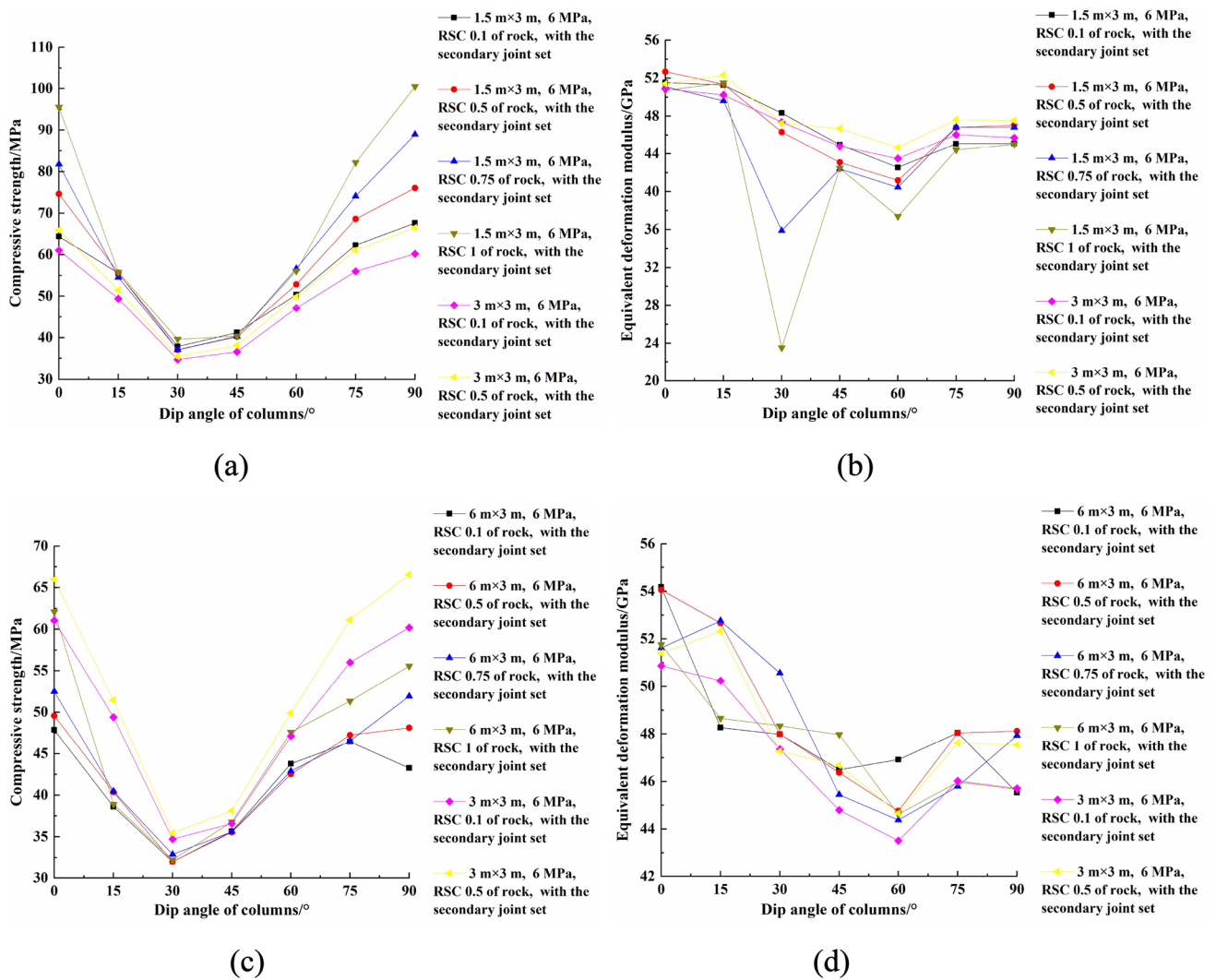


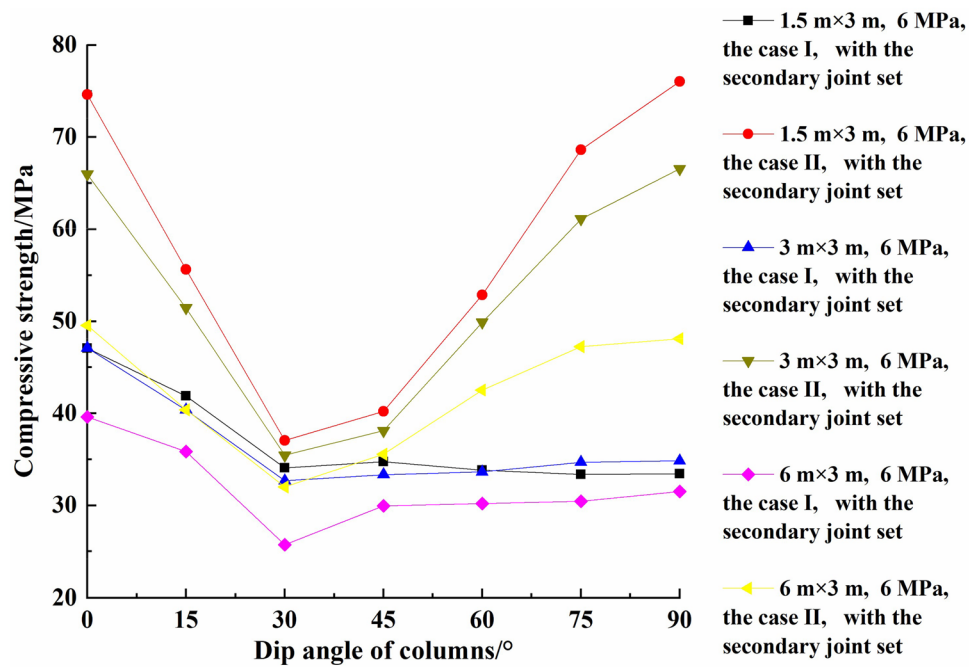
**Fig. 19** The CSs and EDMs when the lateral pressure=6 MPa: **a** and **b** the 1.5 m × 3 m and 3 m × 3 m samples under different residual strength coefficients of rock; **c** and **d** the 3 m × 3 m and 6 m × 3 m samples with under different residual strength coefficients of rock

of 15° and 75°. At the other dip angles, the transverse joints have little effect on the CS. For  $\beta=60^\circ$ , the existence of lateral pressure will weaken the effect of transverse joints on the CSs of the samples.

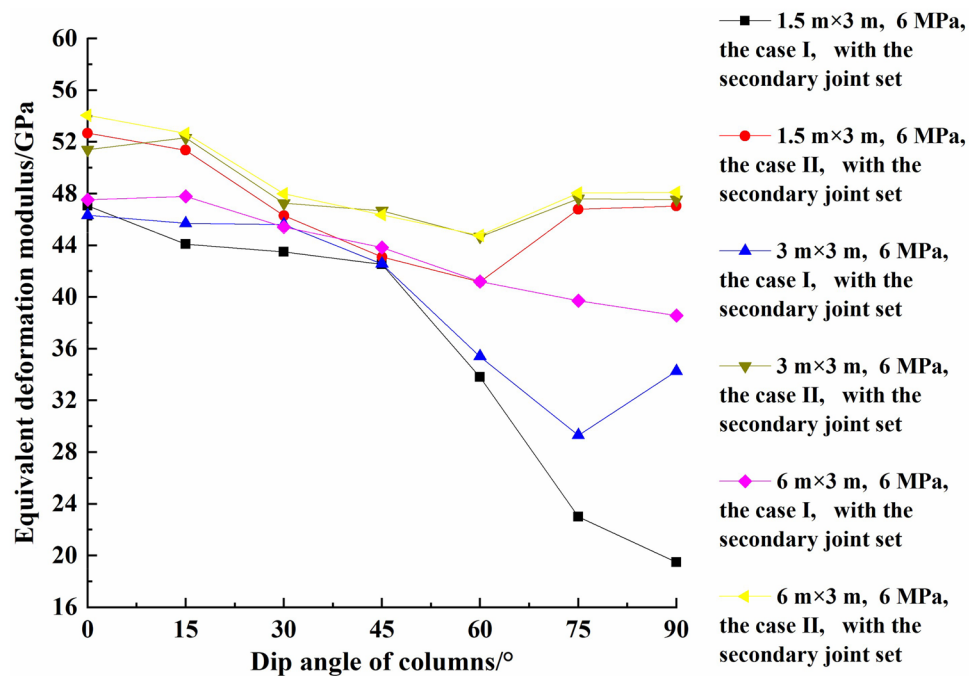
Lin et al. (2018) studied the shape effect of CJRM specimens with transverse joints by the laboratory physical tests and presented the UCS curves of different specimen shapes with various column dip angles. Figure 21a and b compares the simulated results in this paper and the experimental results by Lin et al. (2018). It can be found that they are in relatively good consistency. Clearly, as the dip angle increases, the CSs of the samples change basically in the U-shaped mode. At the dip angle of 60°–90°, the CSs of the samples decrease with the growth of sample height. Ma et al. (2020) applied the equivalent discrete fracture network technology to reveal the deformation of complex fractured rocks. It was found that the total number of cracks is able

to obviously change the magnitude of elastic modulus of fractured rock masses, but the effect on the changing trend is limited. Xiao et al. (2015a, b) gave the continuous failure process of CJRMs subjected to uniaxial compression by the experiments, but the influence of transverse joints was not considered. Xia et al. (2020a, b) discussed the anisotropy and fracture mode of irregular CJRMs subjected to uniaxial compression by the 3D printing technology and compared the strength curve of samples. However, the influence of transverse joints was also not considered in their study. Han et al. (2018) investigated the failure mechanism of intermittent jointed rock masses subjected to biaxial compression by physical tests. However, they did not consider the continuous joints perpendicular to the intermittent joints. Thus, the variation curves of specimen strengths with dip angle are

**Fig. 20** The mechanical properties of the 1.5 m×3 m, 3 m×3 m and 6 m×3 m samples under different model boundaries: **a** compressive strength and **b** equivalent deformation modulus (the case I corresponds to the case between plane stress and plane strain, and the case II corresponds to the case of plane strain)



(a)

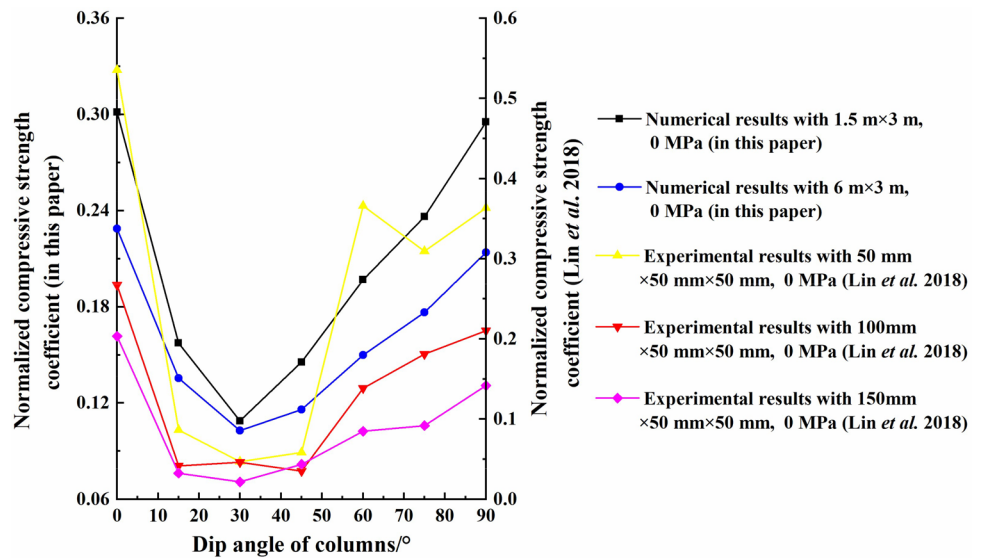


(b)

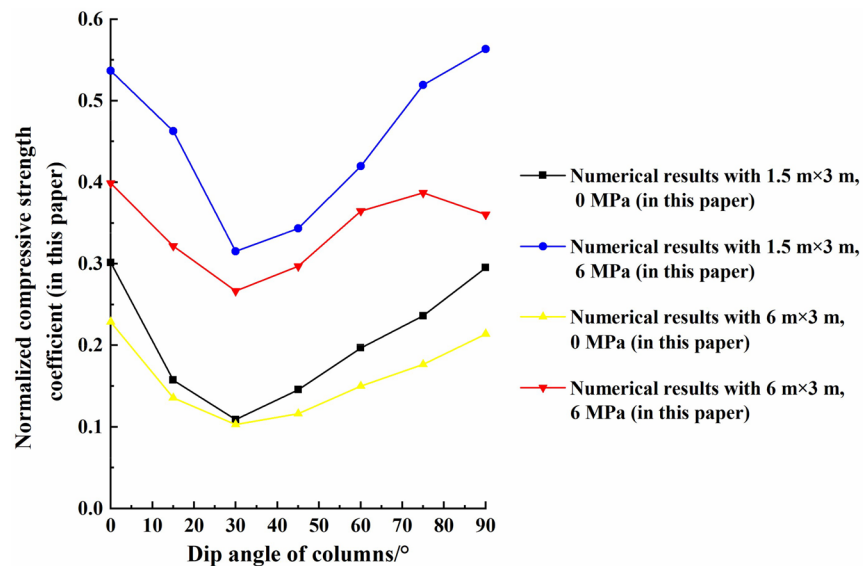
different from the calculated results in this paper. Huang et al. (2020) analyzed the nonlinear deformation behaviors of CJRM under uniaxial compression. However, the influence of transverse joints was also not considered. The research of

Cui et al. (2015) showed that for the CJRM specimens with transverse joints, with the increase of the distance ratio of joint, the EDM first grows and then decreases, which provides insights for understanding the mechanical mechanisms in this study.

**Fig. 21** The normalized compressive strength coefficients of CJBs with transverse joints: **a** comparison of the experimental and simulated results under the lateral pressure of 0 MPa; **b** the simulated results under the lateral pressure of 0 MPa and 6 MPa



(a)



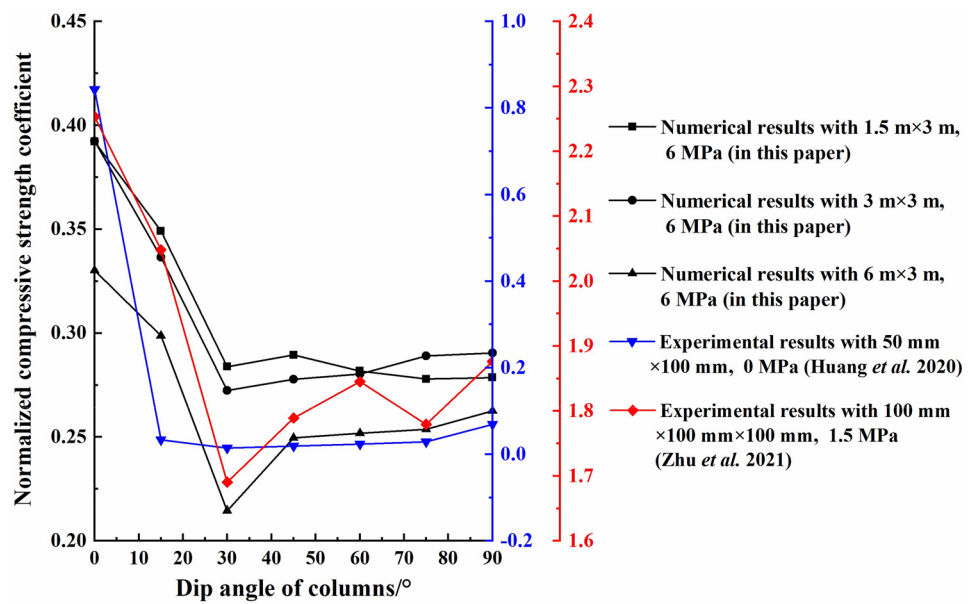
(b)

**4.3 Influence of Model Boundary on Anisotropy and Shape Effect of CJBs with Transverse Joints**

The comparison of the CSs of the 1.5 m x 3 m, 3 m x 3 m and 6 m x 3 m samples with transverse joints and different model boundaries when the lateral pressure = 6 MPa can be summarized as follows: when the case between plane stress and plane strain is considered, for the 1.5 m x 3 m, 3 m x 3 m and 6 m x 3 m samples, as the dip angle increases, the CSs of the samples first decrease quickly and then slowly. Clearly, when the column dip angle exceeds 30°, the CS will change slowly. When the case of plane strain is considered, the CSs of the 1.5 m x 3 m, 3 m x 3 m

and 6 m x 3 m samples change in the U-shape mode as the dip angle increases. The CS of the model equals the minimum at the dip angle of 30°. Figure 22 shows the comparison of the obtained results in this paper and the experimental results by Huang et al. (2020) and Zhu et al. (2021). It can be seen that the change trends show relatively good consistency. However, note that in the study of Huang et al. (2020), the white latex and glue were used as column binder, which were different from the actual joints for CJRMs. Besides, Zhu et al. (2021) produced the column material with gypsum, sand and water by the certain proportion, leading to that the mechanical parameters

**Fig. 22** Comparison of the normalized compressive strength coefficients of CJBs obtained by experiment and simulation



subjected to lateral pressure might be different from the rock material.

## 5 Conclusion

To reveal the anisotropy, shape effect and failure mechanism of CJBs with transverse joints, the meso-mechanics, statistical damage theory and continuum mechanics were modeled in this study. A group of inhomogeneous CJB models with various shapes and transverse joints were established. Under different lateral pressures, the effects of transverse joints, joint mechanical parameters, rock constitutive relations and boundary conditions on the anisotropy, shape effect and energy release characteristics of CJBs were comprehensively analyzed. The key findings are summarized below:

- (1) The anisotropy and shape effect of mechanical properties of CJBs with transverse joints under compression were revealed. As the column dip angle increases, the CSs of samples basically show a U-shaped trend, and as the lateral pressure increases, the CSs of samples at the dip angles of  $0^{\circ}$ – $90^{\circ}$  are obviously improved. ① When the column dip angle is among  $0^{\circ}$ – $90^{\circ}$ , it can be found that the CS of the  $3\text{ m} \times 3\text{ m}$  sample is lower than the  $1.5\text{ m} \times 3\text{ m}$  sample under the lateral pressure of 6 MPa. ② When the column dip angle is  $45^{\circ}$ , the CSs of the  $3\text{ m} \times 3\text{ m}$  and  $6\text{ m} \times 3\text{ m}$  samples show little difference, while for the other dip angles, the CS of the  $3\text{ m} \times 3\text{ m}$  sample is larger. Additionally, the progressive fracture mechanisms and instability precursors of CJBs with different shapes are closely related to the anisotropy and shape effect of mechanical properties of CJBs.
- (2) The transverse joints and lateral pressure have proven to be the critical influence factors for the mechanical properties of CJBs at the certain dip angles of columns. ① In terms of the transverse joints, the CSs of the CJBs with transverse joints are lower than the CJBs without transverse joints at the dip angles of  $0^{\circ}$ ,  $60^{\circ}$  and  $75^{\circ}$  when the lateral pressure = 0 MPa. At the other dip angles, the transverse joints have little effect on the CS. ② In terms of the lateral pressure, the high lateral pressure can reduce the difference between the CSs of the CJBs without and with the transverse joints to a certain degree.
- (3) The change of elastic modulus of joints shows a certain influence on the shape effect of CS and EDM of CJBs at the column dip angle of  $30^{\circ}$  subjected to the lateral pressure of 6 MPa. For the  $1.5\text{ m} \times 3\text{ m}$ ,  $3\text{ m} \times 3\text{ m}$  and  $6\text{ m} \times 3\text{ m}$  CJB samples, the CS will grow with the elastic modulus of joints increases. For the  $1.5\text{ m} \times 3\text{ m}$  CJB sample, the change of the EDM is slow if the elastic modulus of joints exceeds 15 GPa. For the  $3\text{ m} \times 3\text{ m}$  and  $6\text{ m} \times 3\text{ m}$  CJBs, the changes of the EDMs are also gentle if the elastic modulus of joints exceeds 7.5 GPa.
- (4) For the  $1.5\text{ m} \times 3\text{ m}$  CJBs subjected to the lateral pressure of 6 MPa, the residual strength coefficient of rocks has a great influence on the CS at the dip angles of  $0^{\circ}$  and  $75^{\circ}$ – $90^{\circ}$ , while for the  $6\text{ m} \times 3\text{ m}$  CJBs at the dip angles of  $0^{\circ}$  and  $60^{\circ}$ – $90^{\circ}$ , the CSs are greatly affected by the residual strength coefficient of rock.
- (5) The influence of model boundary is significant on the anisotropy and shape effect of the mechanical properties of CJBs under compression. When the case between plane stress and plane strain is considered, for the  $1.5\text{ m} \times 3\text{ m}$ ,  $3\text{ m} \times 3\text{ m}$  and  $6\text{ m} \times 3\text{ m}$  CJB samples,

as the column dip angle increases, the CSs of the CJBs firstly decreases quickly and then gently. But when the case of plane strain is considered, the CSs of the 1.5 m×3 m, 3 m×3 m and 6 m×3 m CJBs change in a U-shape trend as the column dip angle increases.

These achievements will enhance our understanding of fracture mechanisms and failure patterns of CJBs, provide valuable insights into the anisotropy, shape effect and energy release characteristics of CJBs with transverse joints and lay a solid foundation for excavation, support and stability assessment in related engineering.

**Acknowledgements** This study was funded by the National Natural Science Foundation of China (Grant Nos. 42102314 and 42050201) and the China Postdoctoral Science Foundation (Grant No. 2020M680950).

**Author contributions** Conceptualization, BG; formal analysis and investigation, YW and BG; supervision and funding acquisition, BG and CT; software, CT; writing—original draft, YW; writing—review and editing, BG.

**Data availability** The datasets generated and/or analyzed during the current research are available from the corresponding author upon reasonable request.

## Declarations

**Conflict of interest** The authors have no conflicts of interest to declare.

**Open Access** This article is licensed under a Creative Commons Attribution 4.0 International License, which permits use, sharing, adaptation, distribution and reproduction in any medium or format, as long as you give appropriate credit to the original author(s) and the source, provide a link to the Creative Commons licence, and indicate if changes were made. The images or other third party material in this article are included in the article's Creative Commons licence, unless indicated otherwise in a credit line to the material. If material is not included in the article's Creative Commons licence and your intended use is not permitted by statutory regulation or exceeds the permitted use, you will need to obtain permission directly from the copyright holder. To view a copy of this licence, visit <http://creativecommons.org/licenses/by/4.0/>.

## References

- Chen BP, Gong B, Wang SY, Tang CA (2022) Research on zonal disintegration characteristics and failure mechanisms of deep tunnel in jointed rock mass with strength reduction method. *Mathematics* 10(6):922
- Cui Z, Sheng Q, Leng XL (2015) Study on structural effect of equivalent elastic modulus of columnar jointed rock mass. In: *Proceedings of the 3rd International Conference on Machinery, Materials and Information Technology Applications*, Atlantis Press. p 1599–1607
- Cui Z, Wei Q, Hou J, Sheng Q, Li LQ (2016) Structural effect on equivalent modulus of deformation of columnar jointed rock mass with jointed finite element method. *Rock Soil Mech* 37(10):2921–2928+2936

- Fan QX, Wang ZL, Xu JR, Zhou MX, Jiang Q, Li G (2018) Study on deformation and control measures of columnar jointed basalt for Baihetan super-high arch dam foundation. *Rock Mech Rock Eng* 51:2569–2595
- Feng XH, Gong B, Tang CA, Zhao T (2022) Study on the non-linear deformation and failure characteristics of EPS concrete based on CT-scanned structure modelling and cloud computing. *Eng Fract Mech* 261:108214
- Gilman JJ (2009) Basalt columns: large scale constitutional supercooling? *J Volcanol Geoth Res* 184:347–350
- Gong B, Liang ZZ, Liu XX (2022a) Nonlinear deformation and failure characteristics of horseshoe-shaped tunnel under varying principal stress direction. *Arab J Geosci* 15:475
- Gong B, Wang YY, Zhao T, Tang CA, Yang XY, Chen TT (2022b) AE energy evolution during CJB fracture affected by rock heterogeneity and column irregularity under lateral pressure. *Geomat Nat Haz Risk* 13(1):877–907
- Gui Y, Zhao GF (2015) Modelling of laboratory soil desiccation cracking using DLSSM with a two-phase bond model. *Comput Geotech* 69:578–587
- Guy B (2010) Comments on “Basalt columns: large scale constitutional supercooling?” by John Gilman (2009) and presentation of some new data. *J Volcanol Geoth Res* 194:69–73
- Han GS, Jing HW, Jiang YJ, Liu RC, Su HJ, Wu JY (2018) The effect of joint dip angle on the mechanical behavior of infilled jointed rock masses under uniaxial and biaxial compressions. *Processes* 6(5):49
- Huang W, Xiao WM, Tian MT, Zhang LH (2020) Model test research on the mechanical properties of irregular columnar jointed rock masses. *Rock Soil Mech* 41(7):2349–2359
- Ji H, Zhang JC, Xu WY, Wang RB, Wang HL, Yan L, Lin ZN (2017) Experimental investigation of the anisotropic mechanical properties of a columnar jointed rock mass: observations from laboratory-based physical modelling. *Rock Mech Rock Eng* 50:1919–1931
- Jiang Q, Feng XT, Fan YL, Zhu XD, Hu LX, Li SJ, Hao XJ (2013) Survey and laboratory study of anisotropic properties for columnar jointed basaltic rock mass. *Chin J Rock Mech Eng* 32(12):2527–2535
- Jiang Q, Wang B, Feng XT, Fan QX, Wang ZL, Pei SF, Jiang S (2018) In situ failure investigation and time-dependent damage test for columnar jointed basalt at the Baihetan left dam foundation. *Bull Eng Geol Env* 78:3875–3890
- Ke ZQ, Wang HL, Xu WY, Lin ZN, Ji H (2019) Experimental study of mechanical behaviour of artificial columnar jointed rock mass containing transverse joints. *Rock Soil Mech* 40(2):660–667
- Lemaitre J (1992) *A course on damage mechanics*. Springer, Berlin
- Lemaitre J, Desmorat R (2005) *Engineering damage mechanics: ductile, creep and brittle failures*. Springer, Berlin
- Liang ZZ (2005) *Three-dimensional failure process analysis of rock and associated numerical tests*. Ph.D. Thesis. Northeastern University, China, Shenyang
- Lin ZA, Xu WY, Wang W, Wang HL, Wang RB, Ji H, Zhang JC (2018) Determination of strength and deformation properties of columnar jointed rock mass using physical model tests. *KSCE J Civ Eng* 22(7):3302–3311
- Liu XZ, Tang CA, Li LC, Lv PF, Liu HY (2017) Microseismic monitoring and 3D finite element analysis of the right bank slope, Dagangshan hydropower station, during reservoir impounding. *Rock Mech Rock Eng* 50:1901–1917
- Ma GW, Li MY, Wang HD, Chen Y (2020) Equivalent discrete fracture network method for numerical estimation of deformability in complexly fractured rock masses. *Eng Geol* 277:105784
- Mazars J, Pijaudiercabot G (1989) Continuum damage theory-application to concrete. *J Eng Mech* 115(2):345–365

- Simo JC, Ju JW (1987) Strain- and stress-based continuum damage models—I. Formulation. *Int J Solids Struct* 23(7):821–840
- Skrzypek J, Ganczarski A (1999) Modeling of material damage and failure of structures: theory and applications. Springer, Berlin
- Sun PF, Yang TH, Yu QL, Shen W (2012) Numerical research on anisotropy mechanical parameters of fractured rock mass. *Adv Mater Res* 524–527:310–316
- Tang CA, Kou SQ (1998) Crack propagation and coalescence in brittle materials under compression. *Eng Fract Mech* 61(3–4):311–324
- Tang CA, Tang SB, Gong B, Bai HM (2015) Discontinuous deformation and displacement analysis: from continuous to discontinuous. *Sci China Technol Sci* 58:1567–1574
- Wang PT, Yang TH, Xu T, Cai MF, Li CH (2016) Numerical analysis on scale effect of elasticity, strength and failure patterns of jointed rock masses. *Geosci J* 20:539–549
- Wang YY, Gong B, Tang CA, Zhao T (2022) Numerical study on size effect and anisotropy of columnar jointed basalts under uniaxial compression. *Bull Eng Geol Env* 81:41
- Weinberger R, Burg A (2019) Reappraising columnar joints in different rock types and settings. *J Struct Geol* 125:185–194
- Wu N, Liang ZZ, Li YC, Li H, Li WR, Zhang ML (2019) Stress-dependent anisotropy index of strength and deformability of jointed rock mass: insights from a numerical study. *Bull Eng Geol Env* 78:5905–5917
- Xia YJ, Zhang CQ, Zhou H, Chen JL, Gao Y, Liu N, Chen PZ (2020a) Structural characteristics of columnar jointed basalt in drainage tunnel of Baihetan hydropower station and its influence on the behavior of P-wave anisotropy. *Eng Geol* 264:105304
- Xia YJ, Zhang CQ, Zhou H, Hou J, Su GS, Gao Y, Liu N, Singh HK (2020b) Mechanical behavior of structurally reconstructed irregular columnar jointed rock mass using 3D printing. *Eng Geol* 268:105509
- Xiao WM, Deng RG, Fu XM, Wang CY (2014) Model experiments on deformation and strength anisotropy of columnar jointed rock masses under uniaxial compression. *Chin J Rock Mech Eng* 33(5):957–963
- Xiao WM, Deng RG, Fu XM, Wang CY (2015a) Experimental study of deformation and strength properties of simulated columnar jointed rock masses under conventional triaxial compression. *Chin J Rock Mech Eng* 34:2817–2826
- Xiao WM, Deng RG, Zhong ZB, Fu XM, Wang CY (2015b) Experimental study on the mechanical properties of simulated columnar jointed rock masses. *J Geophys Eng* 12:80–89
- Xiao YX, Feng XT, Chen BR, Feng GL, Yao ZB, Hu LX (2017) Excavation-induced microseismicity in the columnar jointed basalt of an underground hydropower station. *Int J Rock Mech Min Sci* 97:99–109
- Xu T, Fu M, Yang SQ, Heap MJ, Zhou GL (2021) A numerical meso-scale elasto-plastic damage model for modeling the deformation and fracturing of sandstone under cyclic loading. *Rock Mech Rock Eng* 54:4569–4591
- Yan DX, Xu WY, Wang W, Shi C, Shi AC, Wu GY (2012) Research of size effect on equivalent elastic modulus of columnar jointed rock mass. *Chin J Geotech Eng* 34(2):243–250
- Yan L, Xu WY, Wang RB, Meng QX (2018) Numerical simulation of the anisotropic properties of a columnar jointed rock mass under triaxial compression. *Eng Comput* 35:1788–1804
- Zavada P, Dedecek P, Lexa J, Keller GR (2015) Devils Tower (Wyoming, USA): a lava coulee emplaced into a maar-diatreme volcano? *Geosphere* 11:354–375
- Zhang K, Liu XH, Liu WL, Zhang S (2021) Influence of weak inclusions on the fracturing and fractal behavior of a jointed rock mass containing an opening: experimental and numerical studies. *Comput Geotech* 132:104011
- Zheng WT, Xu WY, Ning Y, Meng GT (2010) Scale effect and anisotropy of deformation modulus of closely jointed basaltic mass. *J Eng Geol* 18(4):559–565
- Zhou JR, Wei J, Yang TH, Zhu WC, Li LC, Zhang PH (2018) Damage analysis of rock mass coupling joints, water and microseismicity. *Tunn Undergr Space Technol* 71:366–381
- Zhu ZD, Lu WB, He YX, Que XC (2021) Experimental study on the strength failure characteristics of columnar jointed rock masses under three-dimensional stress. *KSCE J Civ Eng* 25:2411–2425

**Publisher's Note** Springer Nature remains neutral with regard to jurisdictional claims in published maps and institutional affiliations.